

Impacts of the Atlantic Multidecadal Variability on North American Summer Climate and Heat Waves

YOHAN RUPRICH-ROBERT

Atmosphere and Ocean Sciences, Princeton University, and NOAA/Geophysical Fluid Dynamics Laboratory, Princeton, New Jersey, and Barcelona Supercomputing Center, Barcelona, Spain

THOMAS DELWORTH

NOAA/Geophysical Fluid Dynamics Laboratory, Princeton, New Jersey

RYM MSADEK

CNRS/CERFACS CECI UMR 5318, Toulouse, France

FREDERIC CASTRUCCIO, STEPHEN YEAGER, AND GOKHAN DANABASOGLU

Global and Climate Dynamics, National Center for Atmospheric Research, Boulder, Colorado

(Manuscript received 25 April 2017, in final form 27 January 2018)

ABSTRACT

The impacts of the Atlantic multidecadal variability (AMV) on summertime North American climate are investigated using three coupled global climate models (CGCMs) in which North Atlantic sea surface temperatures (SSTs) are restored to observed AMV anomalies. Large ensemble simulations are performed to estimate how AMV can modulate the occurrence of extreme weather such as heat waves. It is shown that, in response to an AMV warming, all models simulate a precipitation deficit and a warming over northern Mexico and the southern United States that lead to an increased number of heat wave days by about 30% compared to an AMV cooling. The physical mechanisms associated with these impacts are discussed. The positive tropical Atlantic SST anomalies associated with the warm AMV drive a Matsuno–Gill-like atmospheric response that favors subsidence over northern Mexico and the southern United States. This leads to a warming of the whole tropospheric column, and to a decrease in relative humidity, cloud cover, and precipitation. Soil moisture response to AMV also plays a role in the modulation of heat wave occurrence. An AMV warming favors dry soil conditions over northern Mexico and the southern United States by driving a year-round precipitation deficit through atmospheric teleconnections coming both directly from the North Atlantic SST forcing and indirectly from the Pacific. The indirect AMV teleconnections highlight the importance of using CGCMs to fully assess the AMV impacts on North America. Given the potential predictability of the AMV, the teleconnections discussed here suggest a source of predictability for the North American climate variability and in particular for the occurrence of heat waves at multiyear time scales.

1. Introduction

Heat waves cause catastrophic crop failures, increased mortality from hyperthermia, and widespread power outages due to the increased use of air conditioning. For

example, the severe 2003 European summer heat wave led to 70 000 deaths (Robine et al. 2008), an increase in forest fires (Fischer et al. 2007), and decreased agricultural production (Ciais et al. 2005). Focusing on the United States, Changnon et al. (1996) estimate that about 1000 deaths per year are attributable to heat waves, with particular events such as the 1980 heat wave that impacted the Midwest and the Great Plains causing about 10 000 deaths. Kunkel et al. (1999) and Ross and Lott (2003) further estimate that each severe heat wave episode has inflicted agricultural and industrial damage

Supplemental information related to this paper is available at the Journals Online website: <https://doi.org/10.1175/JCLI-D-17-0270.s1>.

Corresponding author: Yohan Ruprich-Robert, yurprich@bsc.es

DOI: 10.1175/JCLI-D-17-0270.1

© 2018 American Meteorological Society. For information regarding reuse of this content and general copyright information, consult the [AMS Copyright Policy](#) (www.ametsoc.org/PUBSReuseLicenses).

ranging from billions to tens of billions of U.S. dollars. Predicting heat waves, and more specifically their likelihood of occurrence, is a scientific challenge that hence has the potential to enhance our resilience to such extreme climatic hazards.

Heat waves are primarily driven by internal atmospheric variability (Schubert et al. 2011; Dole et al. 2011), but their frequency of occurrence and severity can be modulated by atmospheric boundary forcing. Soil moisture deficits have been shown to play an important role in intensifying heat wave severity (Huang and van den Dool 1993; Fischer et al. 2007; Jia et al. 2016; Donat et al. 2016). Indeed, some of the strongest heat wave events were concomitant with drought conditions (e.g., the 2003 European, 2010 Russian, and 2014 California events; Mazdiyasi and AghaKouchak 2015). During summer, dry soil conditions allow less surface cooling through evaporation, and hence precondition the development of positive temperature anomalies (Alexander 2011). On the other hand, warm surface temperatures increase soil water evaporation, favoring dry conditions. This two-way temperature–evaporation feedback tends to extend and intensify warm and dry conditions, and it explains the link between precipitation deficits and warm conditions over land (e.g., Trenberth and Shea 2005).

Radiative forcing variations, such as those driven by anthropogenic emissions, can also modulate the occurrence of heat waves (e.g., Hansen et al. 2012). Previous studies, based on coupled global climate models (CGCMs) integrated under different anthropogenic forcing scenarios, concluded that over the United States, the number of heat waves would increase during the twenty-first century (Meehl and Tebaldi 2004; Diffenbaugh et al. 2005; Lau and Nath 2012). However, this increasing trend may be modulated by the impacts on land of low-frequency sea surface temperature (SST) variability (e.g., Schubert et al. 2016; Seager and Ting 2017), such as that associated with the internally driven component of the Pacific decadal oscillation (PDO; Newman et al. 2016) or the Atlantic multidecadal variability (AMV; Schlesinger and Ramankutty 1994; Knight et al. 2005). These low-frequency SST variations may explain why there has not been any long-term trend of heat waves detected over the United States during the twentieth century, despite the increase of radiative forcing (Kunkel et al. 1999; Easterling et al. 2000).

The impacts of SST variability on North American temperature and precipitation have been documented by numerous studies. El Niño–Southern Oscillation (ENSO) has a large influence on the annual mean surface temperature and precipitation over North America, with cold tropical Pacific SSTs (i.e., La Niña conditions)

favoring warming and reduced precipitation over Mexico and the southern United States, whereas El Niño conditions are associated with a warming over Alaska and northwestern Canada (Trenberth and Branstator 1992; Trenberth and Guillemot 1996; Mo and Higgins 1998; Seager et al. 2005a). Using an atmosphere-only model forced by observed SST over the tropical Pacific, Seager et al. (2005b) further found that decadal tropical Pacific SST variations are the ultimate drivers of persistent droughts and pluvials over western North America. Schubert et al. (2016) emphasized the seasonality of the climate impacts of the tropical Pacific SST, with the weakest connection to North America occurring in the boreal summer. During this season, the tropical Atlantic appears to be the main SST forcing.

Focusing on the North Atlantic forcing, Sutton and Hodson (2005, 2007) showed, using an atmosphere-only model, that the warm phase of the AMV (referred to as the positive phase or AMV+) tends to create a warming and a precipitation deficit over Mexico and the United States during boreal summer. These results are consistent with the observation-based studies of Enfield et al. (2001) and McCabe et al. (2004), who found that AMV+ is associated with a decrease of the river streamflow and an increased occurrence of droughts over the southwest and central-north United States. Sutton and Hodson (2005, 2007) also highlighted the key role played by the tropical part of the AMV in driving these impacts. The studies of Wang et al. (2008) and Kushnir et al. (2010), focusing respectively on the impacts of the Atlantic warm pool and on the tropical Atlantic SST in atmosphere-only models, corroborate such impacts on precipitation. Wang et al. (2008) and Feng et al. (2011) infer that this precipitation decrease is due to changes in the position and strength of the Caribbean low-level jet and of the Great Plains low-level jet (GPLLJ), both of which transport atmospheric moisture from the tropical Atlantic to the central United States. However, the robustness of this mechanism still needs to be evaluated. Furthermore, the impact of the AMV on the occurrence of heat waves over North America still need to be assessed.

As mentioned above, most of the studies examining the impacts of AMV on North America have used atmosphere-only models. However, several fully coupled studies have recently shown that North Atlantic variations can drive tropical Pacific changes (Dong et al. 2006; Kucharski et al. 2011; McGregor et al. 2014; Ruprich-Robert et al. 2017). A tropical Atlantic warming modifies the boreal summer Walker circulation and accelerates the trade winds over the central Pacific through an atmospheric bridge. This wind change eventually favors the development of La Niña-like

conditions in the following winter (Li et al. 2015; Ruprich-Robert et al. 2017). Furthermore, Mo et al. (2009) and Schubert et al. (2009) estimate that the strongest impacts of SST on North American climate occur when the North Atlantic and the tropical Pacific SSTs show opposite anomalies (see also McCabe et al. 2004; Kam et al. 2014). The results of the above studies suggest that the AMV impacts on North America cannot be ascertained with sensitivity experiments that just employ standalone atmospheric models, as they cannot represent the adjustment of the tropical Pacific to the AMV forcing. In this study, we use fully coupled models (i.e., CGCMs) in order to fully capture the AMV impacts on climate.

Given the potential predictability of low-frequency SST variations, they can be seen as a source of predictability for North American climate variability. Improving our knowledge of the mechanisms associated with AMV teleconnections can help advance the prediction of climate variations on decadal time scales, in particular the variations in the occurrence of extreme weather events such as heat waves and droughts. In this paper, we investigate the impacts of the AMV on the occurrence of North American heat waves, and we explore the physical mechanisms associated with these impacts. The influence of the AMV is estimated using ensemble simulations performed with three different CGCMs, in which the model North Atlantic SSTs are restored to an estimate of the internally driven component of the observed AMV SST anomalies as described in Ruprich-Robert et al. (2017). The paper is organized as follows. The models and methods—including the experimental protocol and datasets used for this study—are introduced in section 2. The impacts of AMV on the boreal summer climate variations over North America are presented in section 3 and their associated mechanisms are investigated in section 4. We discuss and conclude our results in sections 5 and 6.

2. Models, methods, and datasets

We perform idealized experiments using three CGCMs in which the North Atlantic SSTs are restored to a time-independent spatial pattern corresponding to an estimate of the internally driven component of the observed AMV anomaly.

a. Decomposing the internal and forced components of the observed AMV

To decompose the internal and forced components of the AMV, we follow the approach proposed by Ting et al. (2009) updated with the historical simulations of the 36 CMIP5 models and using the observed SST

dataset from the Extended Reconstructed Sea Surface Temperature version 3 (ERSSTv3; Smith et al. 2008), as explained in Ruprich-Robert et al. (2017). Following this method, the internal component of the observed North Atlantic SST index (hereafter referred to as the AMV index for clarity) is estimated as the residual of the observed North Atlantic basinwide averaged SST (0° – 60° N, 75° – 7.5° W) after subtracting the forced component (see Fig. S1a in the online supplemental material). The spatial pattern of the AMV is obtained by regressing the annual mean observed SST at each grid point onto the AMV index (Fig. S1b). Both the AMV index time series and the SST field have been low-pass filtered prior to the regression using a Lanczos filter (21 weights and a 10-yr cutoff period), and the regression has been computed over the 1870–2013 period.

b. Presentation and evaluation of the CGCMs

We use three different CGCMs in this study: GFDL CM2.1, GFDL FLOR, and NCAR CESM1(CAM5) models (referred to hereafter simply as CM2.1, FLOR, and CESM1, respectively). The detailed formulation and simulation characteristics of CM2.1 are described by Delworth et al. (2006) and Wittenberg et al. (2006). The ocean component of CM2.1 has 50 vertical levels and a nominal 1° horizontal resolution, increasing to $1/3^{\circ}$ meridional spacing near the equator. Its atmospheric component consists of 24 vertical levels and 2° latitude \times 2.5° longitude grid spacing. The land surface component is LM2, in which water may be stored in three lumped reservoirs: snow pack, soil water (representing the plant root zone), and groundwater. FLOR, described in Vecchi et al. (2014), has a very similar oceanic component to CM2.1 but higher horizontal ($50\text{ km} \times 50\text{ km}$) and vertical (32 levels) atmospheric resolution and runs on a cubic sphere. Its land surface component is LM3, which includes a multilayer model of snowpack above the soil and a continuous vertical representation of soil water that spans both unsaturated and saturated zones. CESM1 is used with the same components as the long control simulation of the CESM Large Ensemble Project (Kay et al. 2015). All components of CESM1 have approximately 1° horizontal resolution. The atmospheric component CAM5.2 has 30 hybrid vertical levels. The ocean component POP2 uses 60 vertical levels and a meridional mesh refinement down to a quarter of a degree near the equator. The land surface component is CLM4, which includes a multilayer snowpack and a 15-layer soil column coupled to an unconfined aquifer.

Over North America, the three CGCMs simulate reasonable summertime 2-m air temperature climatology compared to observations (Fig. S2). We note

however that FLOR simulates conditions that are too cold (Fig. S2d). The position of the midtroposphere monsoon high is also well reproduced by CM2.1 and CESM1, whereas the latter is shifted southward in FLOR. The mean North American climate biases of FLOR are likely explained by the too cold SST simulated by this model, especially over the North Atlantic (e.g., Pascale et al. 2016).

c. Description of the coupled model experiments

With the three models, we performed two sets of experiments called AMV+ and AMV−, in which the time-invariant¹ SST anomalies corresponding to the positive and negative phases of the AMV index are imposed over the North Atlantic, respectively. In these experiments, the model daily SST is restored to the observed AMV anomalies superimposed on the models' own daily climatology over the North Atlantic region from 0° to 73°N. We use 8° buffer zones over the northern and southern boundaries with a restoring coefficient decreasing by 0.125 per degree of latitude so that a full restoring is performed only between 8° and 65°N. Outside of the restoring region, the models evolve freely, allowing a full response of the climate system. We stress that the goal of our experiments is to estimate the impacts of AMV on the global climate system through its atmospheric teleconnections. We therefore attempt to minimize the impacts of the North Atlantic SST perturbations on the North Atlantic ocean dynamics such as the gyre and overturning circulations. For CESM1 and CM2.1 the imposed SST anomalies correspond to ± 1 standard deviation of the AMV index (i.e., plus or minus the AMV pattern shown in Fig. S1b) and the restoring time scale is 5 days. For FLOR, we slightly modified the experimental protocol to minimize the North Atlantic ocean adjustment in this model [cf. the discussion in Ruprich-Robert et al. (2017)]. The restoring coefficient is relaxed to 15 days and the imposed SST anomalies correspond to ± 1.5 standard deviation of the AMV. This latter change has been made because the weaker restoring coefficient in FLOR otherwise does not yield SST anomalies as strong as in CESM1 and CM2.1 (especially in winter). Furthermore, sea surface salinity is restored in FLOR to values that counterbalance the surface density anomalies generated by SST restoring. We tested the two different experimental protocols with the CM2.1 model, and we found that the conclusions of this article are not impacted by these changes.

With all models we perform large ensemble simulations (100 members for CM2.1, 50 members for FLOR, and 30 members for CESM1) in order to robustly estimate the climate impacts of AMV, and in particular its impacts on the occurrence of weather extremes. To focus on the internal climate response and to capture the potential response and adjustment of other oceanic basins to the AMV anomalies, the simulations have been integrated for 10 years with fixed external forcing conditions at preindustrial levels.

To estimate the climate impacts attributable to the tropical part of the AMV, we performed additional experiments with CM2.1 and CESM1, called Trop_AMV, in which the observed AMV anomalies are restored only over the tropical North Atlantic region (from 0° to 28°N). We also performed another set of experiments with CM2.1 in which, in addition to restoring the North Atlantic SST to the observed AMV anomaly, we restored the SST of the other oceanic basins to their modeled climatology. We call these experiments Damped_Global_AMV. This drastically inhibits the generation of SST anomalies outside of the North Atlantic. Therefore, the comparison between the AMV experiments and the Damped_Global_AMV experiments provides information about the role played by the SST response outside of the North Atlantic on the AMV impacts over land.

d. Observational and reanalysis datasets

As mentioned above, the SST from the ERSSTv3 dataset (Smith et al. 2008) has been used to extract the AMV pattern imposed in the AMV sensitivity experiments. To compare the model outputs with observations, we use the 5° resolution monthly mean 2-m air temperature from the HadCRUTv4 dataset (Morice et al. 2012), the 5° resolution monthly mean sea level pressure from the HadSLP2 dataset (Allan and Ansell 2006), and the monthly mean precipitation from the 2.5° resolution GPCC dataset (Schneider et al. 2015). We also use the atmospheric winds (horizontal and vertical) and specific humidity of the 2° resolution Twentieth Century Reanalysis (20CR; Compo et al. 2011). To estimate the observed changes in heat waves, we use the maximum daily temperature from the 1° resolution Berkeley Earth Surface Temperature (BEST) gridded reconstruction (Rohde et al. 2013). For all these datasets we use the time period covering 1901–2011.

e. Definition of heat waves and number of heat wave days

Following Lau and Nath (2012), for each member of the AMV+ and AMV− ensembles we define a heat

¹ No month-to-month or interannual variation.

wave event as a group of days satisfying the following three criteria:

- T_{\max} must exceed T_1 for at least three consecutive days,
- T_{\max} averaged over the entire event must exceed T_1 , and
- T_{\max} on each day of the event must exceed T_2 ,

where T_{\max} is the daily maximum 2-m air temperature, and T_1 and T_2 are the temperatures corresponding to, respectively, the 90th and 75th percentile of the June–August (JJA) T_{\max} probability density function (PDF) built from the T_{\max} values of all the members of the AMV+ and AMV– simulations.² In the present study, we will focus on the number of days per boreal summer that satisfy the heat wave criteria (hereafter simply number of heat wave days). More specifically, we will focus on how the number of heat wave days changes between the AMV– and AMV+ conditions.

f. Atmospheric moisture transport/divergence estimation and limitations

To understand the mechanism driving the precipitation anomalies detailed in section 4, we investigate the atmospheric moisture transport and divergence. Unfortunately, the moisture transport was not saved online during the model integrations. Hence, we compute it from monthly-mean atmospheric wind, specific humidity, and surface pressure outputs. We acknowledge that the omission of sub-monthly variability may introduce errors in this estimation. In addition, because of data storage requirements, the three-dimensional atmospheric fields from CM2.1 and FLOR were interpolated and saved on 17 vertical levels. Of particular importance here, the degraded temporal and vertical resolutions introduce spurious divergence anomalies over regions of high topography (see, e.g., Seager and Henderson 2013; see also the detailed discussion in the supplemental material). To partly prevent this issue, we compute the atmospheric humidity divergence over the isopressure surface always defined over North America (i.e., above 700 hPa). Note that the anomalies of atmospheric humidity transport below 700 hPa are also computed and discussed.

² As the T_{\max} PDF is defined at each spatial location, our criteria lead to a relative definition of heat wave. The heat wave magnitude (i.e., the average of T_{\max} over the heat wave events) is then expected to be different from one region to another.

3. Results: Description of the AMV impacts on North America

a. Mean response

The differences of JJA 2-m air temperature between the positive and the negative years of the observed AMV (Fig. 1a) indicate that warm AMV states are linked to warmer than usual conditions over all of Mexico and the United States in observations, with maximum anomaly loading found from northern Mexico to the state of South Dakota. However, because of the presence of external forcing variability, we cannot attribute these observed changes solely to AMV. In addition, because of the shortness of the historical record (~110 yr) compared to the AMV period suggested by observations (~60 yr; cf. Fig. S1b), only a few independent samplings are available to study the AMV climate impacts. It is hence very likely that the observed AMV composite shown on Fig. 1a is also polluted by internal climate noise (i.e., other signals than the ones driven by AMV) and does not rigorously isolate the impacts of AMV. To tackle these issues, we investigate the climate impacts of AMV from the idealized AMV experiments performed with the three CGCMs introduced in section 2c. Although shifted by about 5° of longitude to the west, we find that the three models reproduce the magnitude of the observed maximum of the temperature anomaly over southwestern North America (Figs. 1b–d), suggesting that the observed decadal variability of the North Atlantic SST has largely contributed to these land surface anomalies. The link in observations between the AMV and the summer surface temperatures over northern Mexico and the southern United States has already been discussed by Sutton and Hodson (2005). Furthermore, the multimodel studies of Hodson et al. (2010) and Ting et al. (2014) found similar AMV impacts over this region, giving confidence in the robustness of these impacts. However, some discrepancies exist between our models' results over the northern and eastern United States, where CESM1 and CM2.1 tend to reproduce the observed warming whereas FLOR shows a slight cooling. These differences among the models highlight uncertainties as to the effective role played by the observed AMV on driving surface temperature anomalies over these regions.

Associated with the surface warming response to AMV+, the three models simulate negative sea level pressure (SLP) anomalies over North America (Figs. 2a–c), which are part of a broad anomalous cyclonic circulation extending from the subtropical North Atlantic to the eastern subtropical North Pacific. In the three models, the anomalous lower troposphere cyclonic circulation is balanced by an anomalous anticyclonic circulation in

June–July–August 2-meter air temperature AMV+ - AMV-

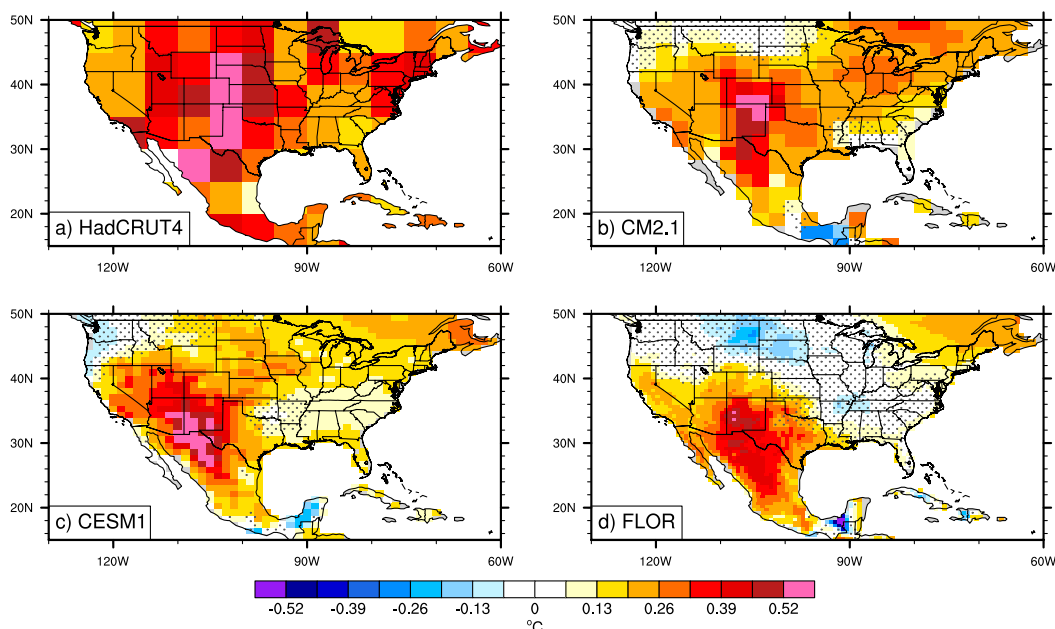


FIG. 1. JJA averaged 2-m air temperature differences between the positive and the negative phase of AMV. (a) Observed temperature composite difference between the positive and the negative years of the observed AMV index (cf. Fig. S1a; dataset: HadCRUT4). The other panels show the temperature difference between the 10-yr ensemble mean average of the AMV+ and AMV- experiments for (b) CM2.1, (c) CESM1, and (d) FLOR. Stippling indicates regions that are below the 95% confidence level of statistical significance according to a two-sided t test.

the upper troposphere, as shown by the wind streamfunction anomalies in Figs. 2e–g. These opposite anomalies between the lower and the upper subtropical troposphere are consistent with a Matsuno–Gill atmospheric response (Matsuno 1966; Gill 1980) to the warming imposed over the tropical North Atlantic. Indeed, we find that the SST warming associated with AMV+ drives anomalous upward motions in the upper troposphere around 10°N over a region extending from the Atlantic to the eastern tropical Pacific (Figs. 2e–g),³ indicating a strengthening of the atmospheric deep convection there. The anomalous deep convection in the tropics generates a tropical Rossby wave–like circulation pattern as well as downward motions north and west of the heating region. Similar results are found in the Trop_AMV experiments (cf. section 2c), confirming that this atmospheric response comes from the tropical part of the AMV forcing (Fig. S3). Our results are consistent with the study of Sutton and Hodson (2007), who also found that an AMV warming drives anomalous

atmospheric downward motions west of the United States and over northern Mexico.

The observations show also negative SLP anomalies associated with an AMV warming over the broad subtropical North Atlantic–eastern North Pacific region (Fig. 2d), although the magnitude of the SLP anomalies is weaker than the model ones, especially over Mexico and the Caribbean Sea. The AMV composite from the Twentieth Century Reanalysis shows indications of a tropical Rossby wave–like pattern generated over the tropical Atlantic, as well as a predominance of anomalous downward motions in the upper troposphere over southwestern North America (Fig. 2h). The anomalous anticyclonic upper tropospheric circulation in the reanalysis is, however, shifted northward compared to the models' results, and it appears mixed with an extratropical anomaly. Possible explanations for this discrepancy between the CGCMs and the reanalysis can come from the presence of extratropical atmospheric noise and/or external forcing variations in the reanalysis composite. But, it can also indicate a misrepresentation by the CGCMs of the AMV impacts on atmosphere due to common model biases, such as the location of the Gulf Stream separation and its eastward extension, or the

³ In FLOR, the vertical wind has been computed from the divergence of the horizontal winds.

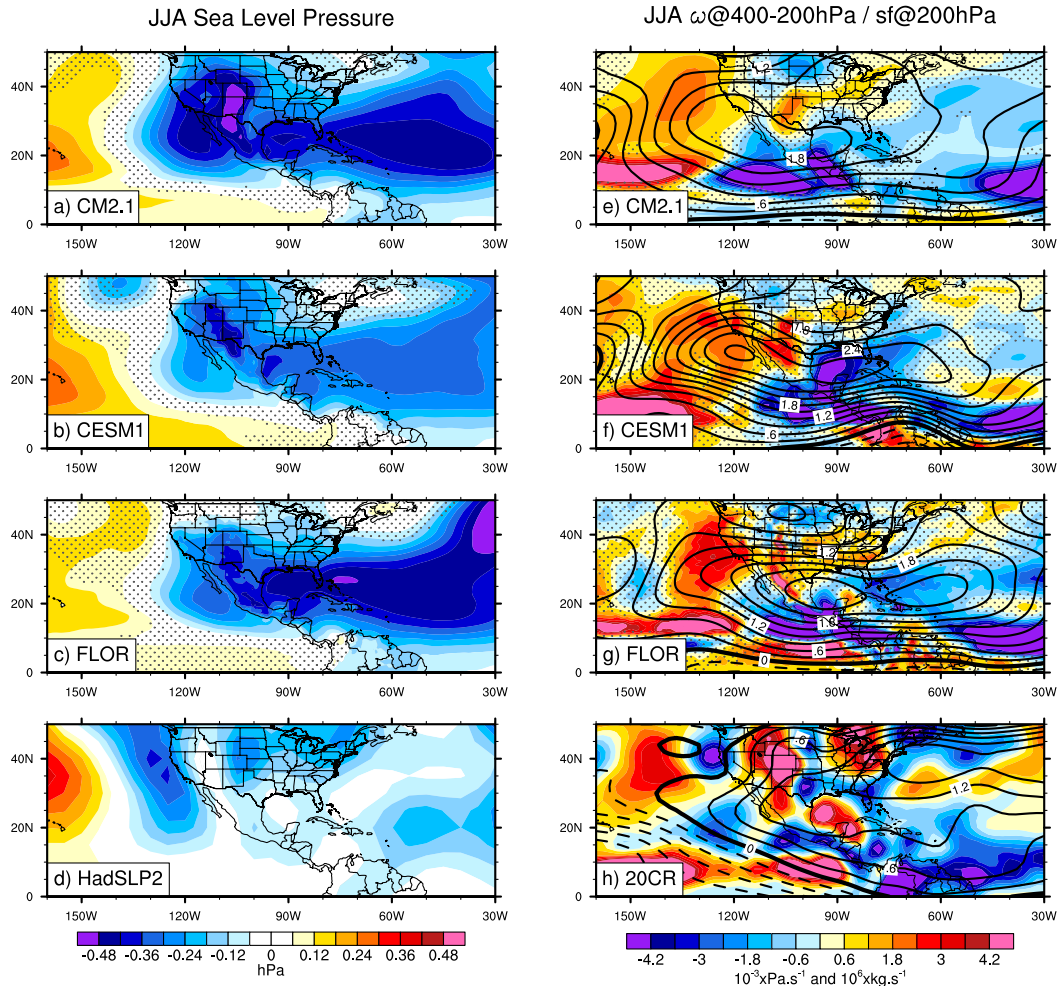


FIG. 2. Differences in 10-yr JJA average sea level pressure between AMV+ and AMV- experiments from (a) CM2.1, (b) CESM1, and (c) FLOR. (d) Observed sea level pressure composite difference between the positive and the negative years of the observed AMV index (dataset: HadSLP2). (e)–(h) As in (a)–(d), but for the vertical atmospheric motion ω averaged between 400 and 200 hPa (shading; positive values mean downward motion) and for the atmospheric streamfunction (sf) at 200 hPa (contours at intervals of $0.3 \times 10^6 \text{ kg s}^{-1}$; positive values indicate anticyclonic circulation; observed dataset: 20CR). Stippling indicates regions that are below the 95% confidence level of statistical significance according to a two-sided t test.

misrepresentation of low cloud over the tropical Atlantic. Further investigations that are beyond the scope of this paper would be needed to test these hypotheses.

b. Heat wave response

The large ensemble simulations performed with the three models allows us to estimate, without any statistical assumptions (such as Gaussian distribution), the modulation of the occurrence of weather extremes by AMV. We focus here on the number of heat wave days per summer (cf. definition in section 2e). Figures 3b–d show that, over northern Mexico and the southwestern United States, the three models simulate an increase of the number of heat wave days per summer with

differences larger than 3 days over some areas, which corresponds to a relative increase of $\sim 30\%$ (cf. climatological values in Figs. S4b–d). We note that these relative changes are robust through heat wave definitions (cf. Fig. S5) and appear insensitive to the mean model climatological biases (Figs. S4b–d). For comparison, Lau and Nath (2012) analyzed the A1B twenty-first-century anthropogenic emission scenario using CM2.1 and found an increasing trend per decade of about 5 heat wave days per summer over North America. Assuming a step shift from a 10-yr (20 yr) period in a given phase of the AMV to a 10-yr (20 yr) period in the other AMV phase, a change of 3 heat wave days translates to a trend per decade of 2.25 days (1.125 days).

June–July–August number of Heat Wave days

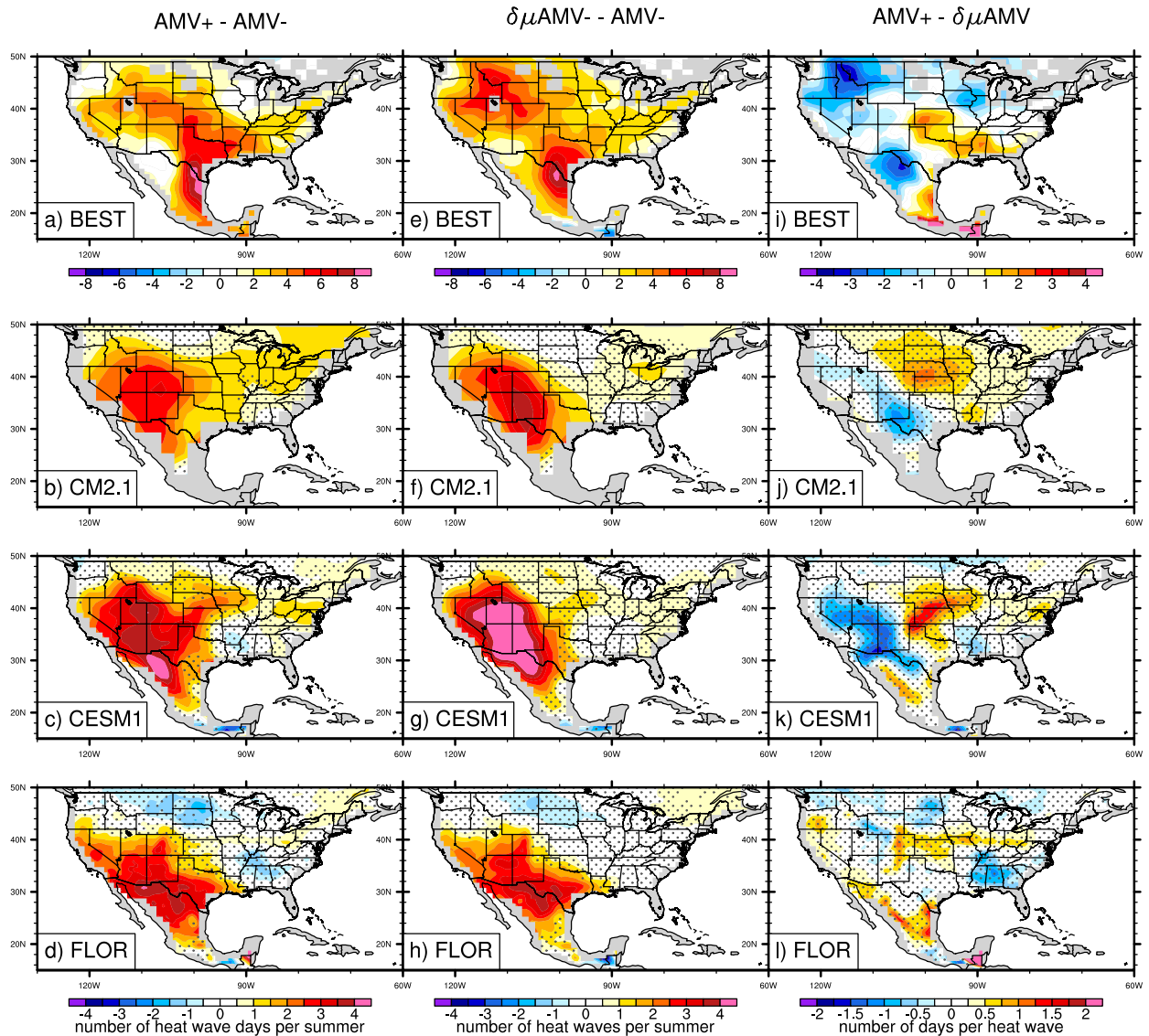


FIG. 3. JJA averaged differences of the number of heat wave days between the positive and negative phases of AMV. (a) Observed number of heat wave day composite difference between the positive and negative years of the observed AMV index (dataset: BEST). Differences in 10-yr average number of heat wave days between AMV+ and AMV- experiments for (b) CM2.1, (c) CESM1, and (d) FLOR. (e)–(h) As in (a)–(d), but for the difference between $\delta\mu\text{AMV-}$ and AMV- conditions (see text for explanations). (i)–(l) As in (a)–(d), but for the difference between AMV+ and $\delta\mu\text{AMV-}$ conditions. The gray regions in (a) are regions where the BEST data are not covering the full 1901–2011 period. The heat wave day changes from models' outputs [all panels except (a), (e), and (i)] are shown for grid cells containing only land surface area. Stippling on panels for model output indicates regions that are below the 95% confidence level of statistical significance according to a two-sided t test. Note the different scale between the top row and the three other rows.

It suggests that AMV can modulate the anthropogenic trend by 45% (22.5%) over a period of 20 yr (40 yr), either reducing or adding up to its effects.

Given the increase in the mean surface temperature over North America from AMV- to AMV+ conditions (cf. Fig. 1), the increase in the number of heat wave days was also to be expected. Here we estimate whether the

increased number of heat wave days can be explained by a simple shift in the distribution of the daily maximum air temperature (the PDF of T_{max}) or if it corresponds also to a change in the shape of the distribution and/or to a change in the persistence of anomalously warm conditions. To do so, we compute, using daily data, the mean seasonal cycle of the daily maximum air

temperature from, on the one hand, all the AMV+ members, and on the other hand, all the AMV− members. We compute the difference between these two seasonal cycles and add this difference to the daily T_{\max} values of each AMV− ensemble members, in order to build a “mean shifted” AMV− distribution. We call this resulting distribution $\delta\mu\text{AMV−}$. Using the same heat wave definition as previously, we count the number of heat wave days in $\delta\mu\text{AMV−}$. We find that the $\delta\mu\text{AMV−}$ distribution broadly reproduces the AMV+ occurrence of heat wave days for FLOR (Figs. 3d,h,l). It indicates that, for this model, the increase of heat wave days from AMV− to AMV+ conditions is consistent with a simple shift in the T_{\max} distribution. There are, however, regions with statistically significant differences between AMV+ and $\delta\mu\text{AMV−}$ for CM2.1 and CESM1, which is particularly true for extremely warm heat waves (Fig. S5). Over the southwestern United States, the number of heat wave days increases less than what was expected from a simple shift of the T_{\max} distribution, whereas over Nevada to Nebraska it increases more. These indicate changes in the T_{\max} PDF shape and/or in the persistence of anomalously warm conditions, which is possibly linked to soil moisture anomalies [cf. section 4b (2); Berg et al. 2014; Douville et al. 2016].

As for the model outputs, we compute the differences of number of heat wave days between the positive and the negative years of the observed AMV using the BEST reconstruction. Similarly to HadCRUT4, the BEST dataset shows an increase of the JJA 2-m air temperature over North America associated with AMV+, but with maximum anomalies slightly shifted to the east (not shown). The BEST composite shows also an increase of the number of heat wave days over Mexico and the United States (Fig. 3a). However, there is an absence of anomalies over the northwest of Mexico and maximum anomalies are found around the Gulf of Mexico and over the Great Plains, which contrasts with our models’ results. In addition, the magnitude of the observed differences of number of heat wave days from BEST is about 2 times as high as the differences found between the ensemble means of our AMV simulations. We test whether these discrepancies are potentially related to observational estimate uncertainties (cf. the supplemental material). We find that, although some discrepancies exist about the precise intensity and location of the heat wave changes, the observed datasets tend to agree on the absence of signal over the northwest of Mexico and on the number of heat wave days increase over the western United States (Fig. S6). It is hence possible that the discrepancies between the observed composite and the model results come from common model incapacities to fully represent the

mechanisms by which AMV modulates heat waves over North America. It is also possible that the observed composite is polluted by external forcing variability or by climate noise. We find indeed that, for the three CGCMs, subsamples of only five members from AMV+ and AMV− simulations can present similar results to the observed composite (Figs. S7g–i).⁴ More generally, the analysis of the signal-to-noise ratio of the AMV impacts shows that ~25% of the decadal variance of the number of heat wave days over southwestern North America is imputable to AMV, the other ~75% being controlled by climate noise (Figs. S7d–f).

4. Mechanisms associated with the AMV impacts: Role of the atmospheric humidity

In this section we investigate the physical mechanisms linking the AMV to the surface temperature variations over North America. According to the Stephan–Boltzmann law, the amount of longwave radiation emitted from the surface is a fourth-power function of the land surface temperature. Further, considering the heat capacity of the land surface as negligible, we can assume that at equilibrium the sum of the surface heat fluxes is equal to 0. It follows that

$$\Delta(T_s) \propto \Delta(\text{LW}_{\text{up}}) = \Delta(\text{SW}_{\text{net}}) + \Delta(\text{LW}_{\text{dn}}) + \Delta(\text{SH}) + \Delta(\text{LH}) + \Delta(G),$$

where $\Delta(\cdot)$ refers to the difference between AMV+ and AMV− conditions, T_s is the land surface temperature, LW_{up} is the outgoing longwave radiation emitted by the surface, SW_{net} is the net shortwave radiation incoming to the surface, LW_{dn} is the longwave radiation incoming to the surface, SH is the sensible heat fluxes, LH is the latent heat fluxes, and G is the heat fluxes penetrating into the ground. For all surface heat fluxes, we choose as convention that positive values represent fluxes going into the land surface. We find that changes in G are one or two orders of magnitude smaller than the changes in the other heat fluxes (not shown), and therefore we do not discuss further its contribution to the surface temperature changes.

Figure 4 shows the JJA anomalies of each of the surface heat flux components over North America. Overall, the land surface heat budget shows that the summer surface warming over northern Mexico and the southwestern United States shown in Fig. 1 is driven by an increased net solar radiation at the surface (SW_{net}) and

⁴This number (5) of members is chosen in order to match the observed sampling (5 members \times 10 yr \times 2 = 100 yr).

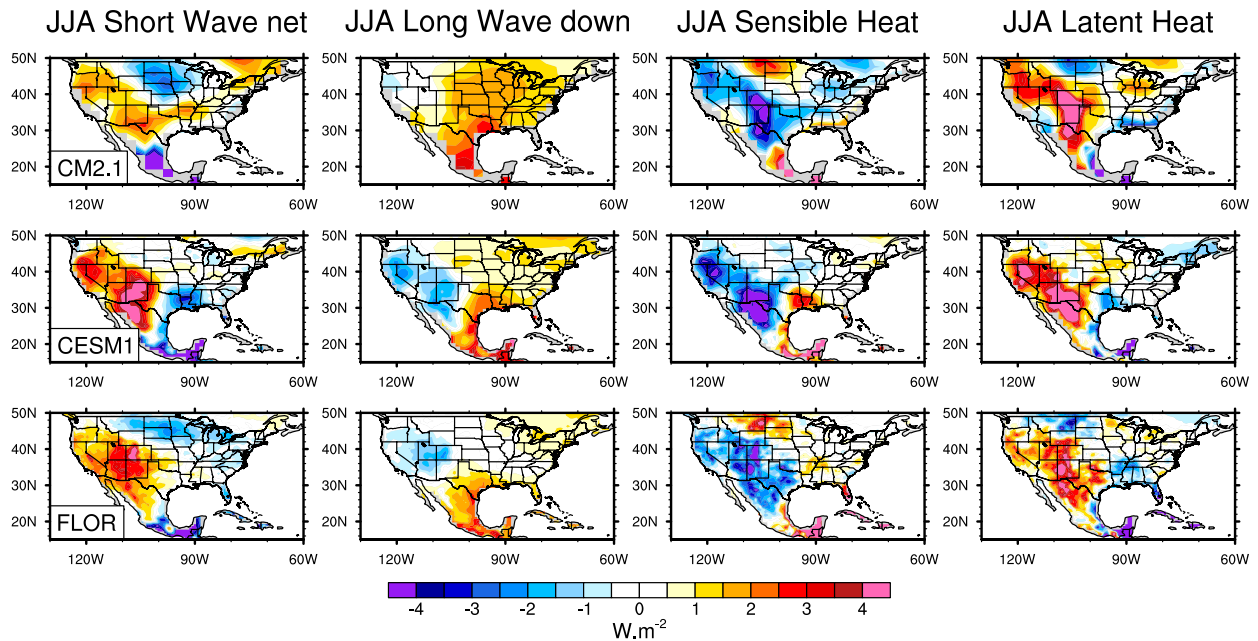


FIG. 4. Differences in 10-yr JJA average surface flux differences of (left to right) net shortwave radiation, downward longwave radiation, sensible heat, and latent heat between AMV+ and AMV- experiments from (top to bottom) CM2.1, CESM1, and FLOR. Positive values indicate a surface warming, by convention. The fluxes are shown for grid cells containing only land surface area.

by decreased surface latent heat flux from the drier land state (LH, which has climatological negative values). Along the coast of the Gulf of Mexico, the surface is warmed by LW_{dn} . This is consistent with the increased of atmospheric humidity here (Fig. 5). Over the northeastern United States, the warming simulated by CM2.1 and CESM1 is also mostly explained by LW_{dn} anomalies, which are mostly absent in FLOR (cf. further details in section 4c), explaining the differences of 2-m air temperature anomalies seen in Figs. 1b–d and potentially the differences in the changes in the number of heat wave days seen in Figs. 3b–d. We discuss in the following sections the physical mechanisms responsible for each of these surface heat flux anomalies.

a. Increase of the incoming solar radiation

Changes in SW_{net} can either come from changes of the surface albedo or from changes in the amount of shortwave radiation that reaches the surface (SW_{dn}). In the present case, the modifications of surface albedo due to the vegetation response in FLOR and CESM1 (the two models including vegetation variations) explain less than 10% of the SW_{net} changes. We find that an AMV warming leads to decrease of both atmospheric humidity and cloud cover over southwestern North America in the three models (Fig. 5). The increase of SW_{net} from AMV- to AMV+ conditions is mostly induced by reduced cloudiness leading to a reduction in atmospheric

albedo, which leads to an increase of SW_{dn} . We argue in the following that these responses are linked to a thermal low atmospheric adjustment to the tropical SST forcing imposed over the North Atlantic.

As introduced in section 3a, the tropical SST warming associated with AMV+ drives a Matsuno–Gill-like atmospheric response, which favors downward motion in the upper troposphere over northern Mexico and the southwestern United States (Figs. 2e–g and 6a). This downward motion tends to warm the upper to mid-troposphere (adiabatic compression), which leads to a decrease of atmospheric relative humidity (Figs. 6b,c). This explains part of the cloud cover decrease (Figs. 5d–f) and the SW_{dn} increase over northwestern Mexico and the southwestern United States. The induced surface warming and subsequent increase of upward longwave radiation lead to a warming of the low and middle troposphere, likely contributing to the fairly homogenized profiles of temperature and relative humidity anomalies over the entire troposphere (Figs. 6b,c). In the three models, we note that anomalous downward motion also occurs over the Pacific Ocean west of the United States. This also likely plays a role in the decrease of relative humidity in the upper atmosphere over the western United States through lateral advection of warm air.

We can infer from the atmospheric vertical velocity anomalies shown in Fig. 6a that the midtroposphere exhibits anomalous horizontal divergence. Combined

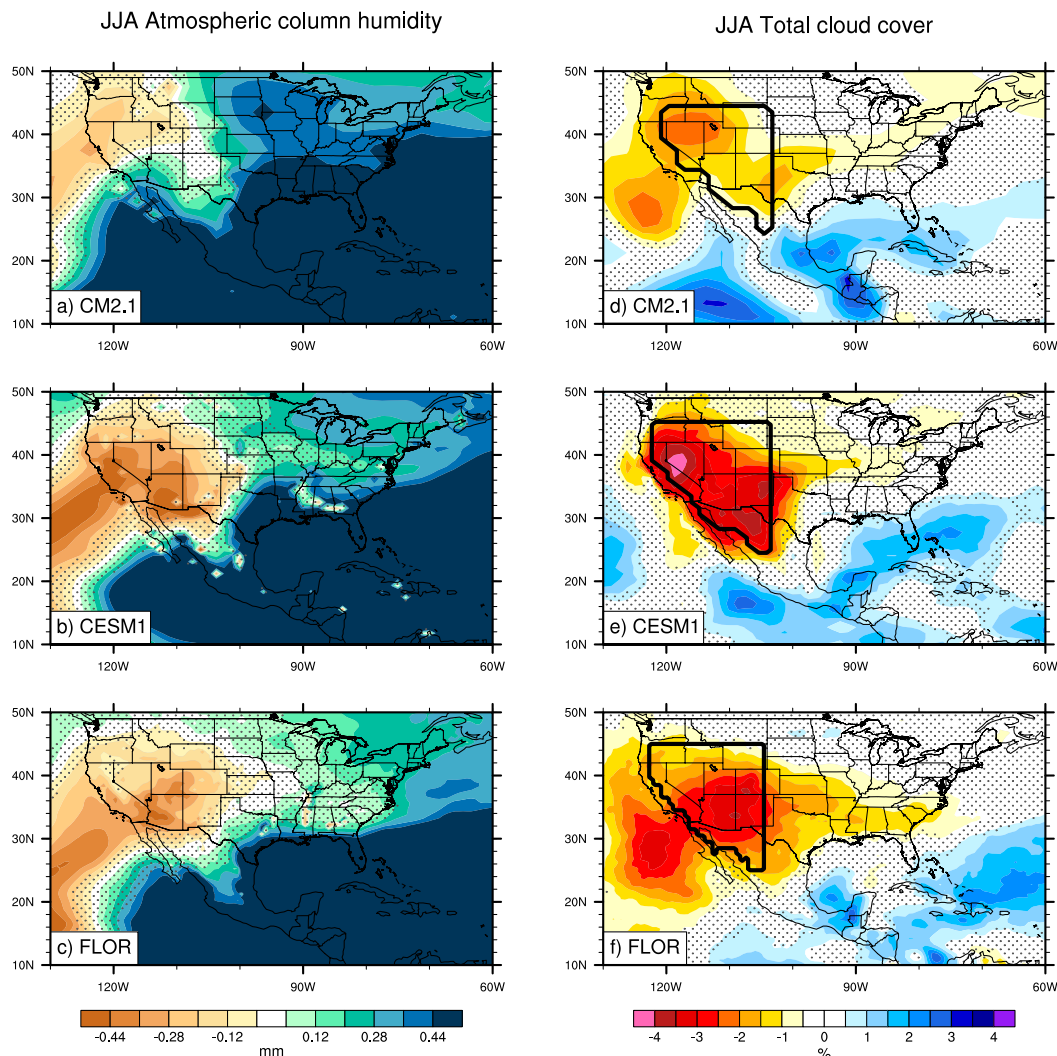


FIG. 5. Difference in 10-yr JJA average vertically integrated atmospheric humidity between AMV+ and AMV– experiments from (a) CM2.1, (b) CESM1, and (c) FLOR. (d)–(f) As in (a)–(c), but for the total atmospheric cloud cover. Stippling indicates regions that are below the 95% confidence level of statistical significance according to a two-sided t test. The thick black contours in (d)–(f) indicate the domain used to compute the profiles shown in Fig. 6. Note that these profiles are computed over land surface area only. The contour differences among the models reflect coastal shape differences due to different atmospheric–land model resolutions.

with the climatological upward motion present in the lower troposphere (and with the positive upward motion anomalies in the CESM1 experiments), this horizontal divergence can act as a sink of moisture for the lower troposphere, leading to negative specific humidity anomalies below 500 hPa (Fig. 6d). These anomalies contribute also to the decrease of relative humidity shown in Fig. 6c and to the decrease of cloud cover discussed above (Figs. 5d–f). We note that CESM1 and FLOR simulate a specific humidity decrease of about 0.1 g kg^{-1} , whereas CM2.1 tends to simulate an anomaly of opposite sign around the surface. This difference comes from the month of August during which CM2.1

simulates a significant wetting of the atmosphere unlike CESM1 and FLOR (Fig. 6d).

Divergence of humidity in the lower troposphere may also happen very locally over important moisture source regions such as the Gulf of California. Over this region, moisture surges with a typical one-week time scale play an important role in the amount of humidity transported from the Gulf of California to northern Mexico and the southwestern United States (e.g., Pascale et al. 2016). Unfortunately, in the present case we do not have high enough three-dimensional temporal resolution outputs of humidity and wind (i.e., 6 hourly or daily) at our disposal to investigate this

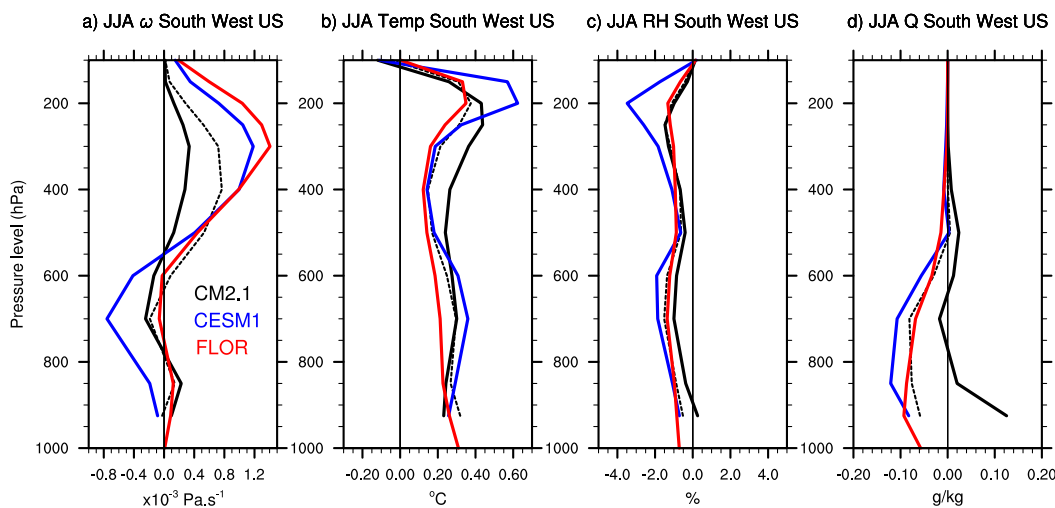


FIG. 6. Differences in 10-yr JJA average of vertical atmospheric profiles averaged over the broad southwestern U.S. region indicated in Fig. 5 for (a) vertical motion, (b) temperature, (c) relative humidity, and (d) specific humidity from CM2.1 (black line), CESM1 (blue line), and FLOR (red line). The dashed black lines represent the June–July differences from CM2.1. Positive anomaly of vertical motion means increased upward motion.

potential contribution to the negative specific humidity anomalies (cf. section 2f).

b. Decrease of latent heat loss

The latent heat flux is directly linked to the evaporation–sublimation fluxes. The positive latent heat flux anomalies shown in Fig. 4 hence correspond to negative JJA evaporation anomalies over northern Mexico and southwestern United States in response to an AMV warming. This decrease of JJA evaporation can either come 1) from concomitant changes of atmospheric conditions such as JJA precipitation, wind, humidity, and temperature or 2) from a negative anomaly of precipitation minus evaporation budget earlier in the year, which would lead to less soil moisture to be potentially evaporated during the summer. We investigate these two possibilities in what follows.

1) JJA ATMOSPHERIC CONDITIONS

As shown previously, positive temperature anomalies (Fig. 1) and negative atmospheric humidity anomalies (Figs. 5 and 6) prevail over southwestern North America. Furthermore, we find that the strength of the surface winds tends to increase over this region (not shown). These above mentioned atmospheric anomalies should drive an increase in evaporation. We can hence conclude that these three factors are working to counteract the LH anomalies over North America seen in Fig. 4. On the other hand, Figs. 7a–c show a decrease of precipitation over the entire northern Mexico and southwestern United States, with maximum anomalies localized over the Sierra Madre

Occidental and the Rocky Mountains. This indicates that JJA precipitation anomalies play an important role in the LH anomalies seen in Fig. 4.

The mass divergence prevailing in the midtroposphere over southwestern North America (cf. Fig. 6a) may explain these precipitation anomalies. We find indeed that positive anomalies of horizontal humidity divergence in the midtroposphere (Figs. 7e–g) are collocated with negative precipitation anomalies (Figs. 7a–c). Surprisingly, there is a strong agreement among the models in terms of humidity divergence, whereas models disagree on the horizontal humidity transport. It suggests that the horizontal divergence anomalies are primarily driven by the anomalous subsidence shown in Figs. 2e–g, and that the horizontal midtroposphere dynamic is not key to understanding the JJA North American precipitation response to AMV. However, as warned in section 2f, the atmospheric moisture transport and divergence are computed from monthly mean wind and humidity fields. They are therefore subject to errors due to the omission of submonthly variations (cf. the online supplemental material; see Figs. S9 and S10 for an estimate of these errors). Nevertheless, results from Figs. 7a–c and 7e–g suggest that the JJA dynamical atmospheric response to AMV plays a role in the precipitation deficit over this region.

By decomposing the humidity divergence anomalies $[\Delta \text{div}(q\mathbf{u})]$ into a part coming from wind anomalies $[\text{div}(q\Delta\mathbf{u})]$ and a part coming from humidity anomalies $[\text{div}(\mathbf{u}\Delta q)]$, we find that the anomalous humidity divergence in the midtroposphere is mainly explained by

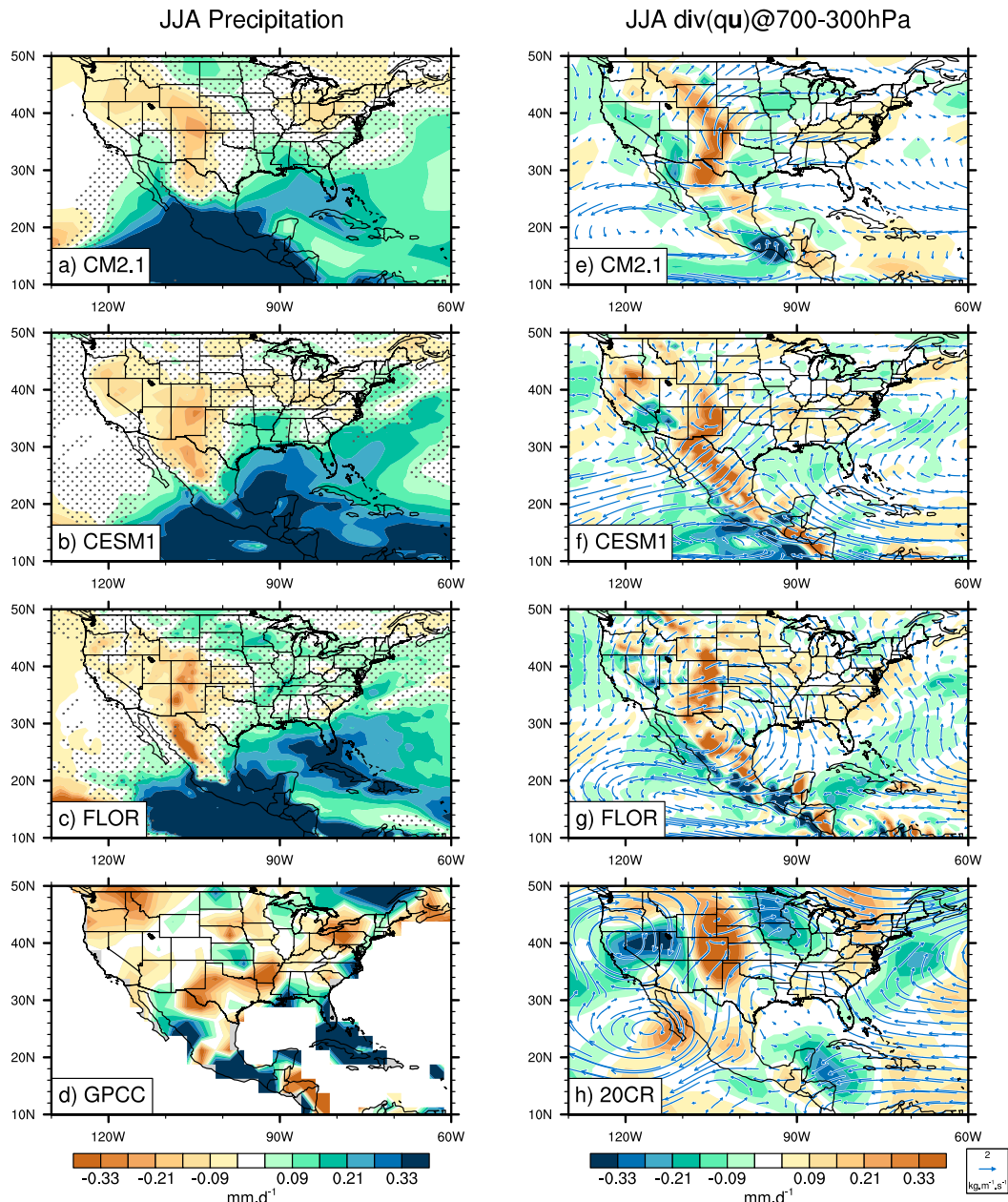


FIG. 7. JJA averaged differences of precipitation and midtroposphere moisture divergence between the positive and the negative phase of AMV. (a) Observed precipitation composite difference between the positive and the negative years of the observed AMV index (dataset: GPCC). Also shown are differences in 10-yr JJA precipitation between AMV+ and AMV− experiments from (b) CM2.1, (c) CESM1, and (d) FLOR. (e)–(h) As in (a)–(d), but for the atmospheric specific humidity divergence (shading) and transport (vectors) integrated over 700 and 300 hPa (observed dataset: 20CR). Stippling in (b)–(d) and (f)–(h) indicates regions that are below the 95% confidence level of statistical significance according to a two-sided t test.

the wind anomalies south of 35°N (Fig. S8). Under the assumption that the atmospheric dynamics is not impacted by the atmospheric humidity anomalies, it confirms that the JJA atmospheric circulation response to AMV (cf. section 4a) is driving the negative JJA precipitation anomalies over this region. North of

35°N , atmospheric humidity anomalies seem to explain the JJA precipitation deficits (Fig. S8), but their impact on precipitation appears to be counteracted by the wind anomalies (especially for CM2.1 and CESM1). Understanding the causes of atmospheric humidity anomalies is not trivial as these anomalies are a function

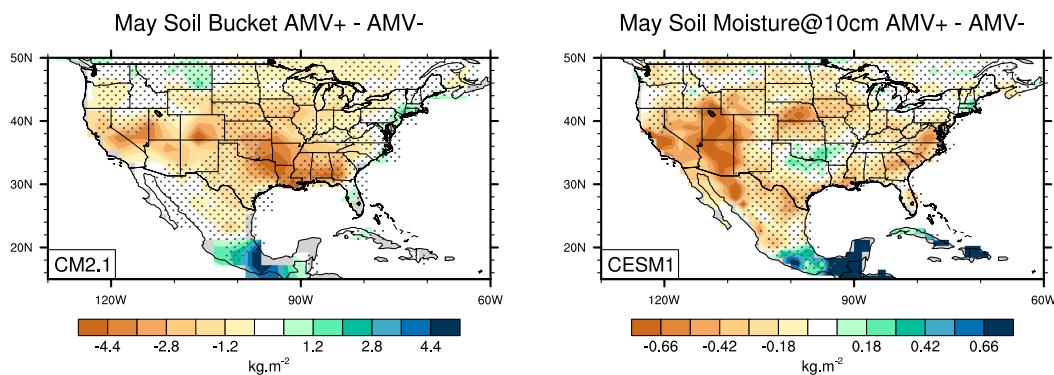


FIG. 8. Differences in 10-yr May average soil moisture between AMV+ and AMV- experiments from (a) CM2.1 and (b) CESM1. For CM2.1 the soil moisture anomalies have been computed over to the entire plant root zone (bucket), whereas for CESM1 these anomalies are shown for the single 10-cm level. Stippling indicates regions that are below the 95% confidence level of statistical significance according to a two-sided t test.

of evaporation, precipitation,⁵ and atmospheric humidity divergence anomalies (implying nonlinearities). Detailed investigation of the relative role played by these different factors would require further sensitivity experiments that are beyond the scope of this study [e.g., preventing soil moisture feedback on precipitation, as discussed in Schubert et al. (2004)]. However, we note that the regions where the atmospheric humidity anomalies play an important role correspond to the regions with strong coupling strength between precipitation and soil moisture, as identified by Koster et al. (2004). This suggests that JJA precipitation anomalies shown in Figs. 7a–c may partly be induced or amplified by JJA soil moisture anomalies.

We also investigate from observational estimates the AMV composite of JJA precipitation and atmospheric humidity transport/divergence.⁶ We find anomalous midtroposphere humidity divergence similar to the models' ones over the Rocky Mountains and Mexico (Fig. 7h). There is, however, no precipitation anomaly over the Rocky Mountains (Fig. 7d). To the extent that the comparison between models, experiments, and observations is fair, the absence of link between midtroposphere humidity divergence and rainfall anomalies over southwestern North America in observations suggests that the precipitation response to AMV may have been counteracted by submonthly variations of the

atmospheric humidity transport. However, it can also come from inconsistency between the two observational estimate databases. The absence of precipitation anomalies in the observed AMV composite further indicates that the temperature and heat wave anomalies seen in Figs. 1a and 3a cannot be explained by JJA precipitation changes, which contrasts with our models' results.

2) SOIL MOISTURE

As stated above, JJA evaporation anomalies may also come from a lack of soil moisture at the beginning of the summer, which would result from negative anomaly of the land water budget earlier in the year. To verify this hypothesis, we have at our disposal soil moisture outputs from just CESM1 and CM2.1. For these models, we find that the soil tends to be already drier than usual at the beginning of the summer in response to an AMV warming (Fig. 8). These soil moisture anomalies are consistent with a deficit of precipitation between September and May (cf. Figs. 9a,b). We note that the 9-month-mean precipitation anomalies shown in Figs. 9a–c can be easily linked to the so-called standardized precipitation index (SPI; e.g., Hayes et al. 2000) used to monitor droughts. Mo and Schemm (2008) found a good agreement over northern Mexico and the western United States between soil moisture anomalies and SPI computed from 6 months of precipitation anomalies (cf. Fig. 2 in Mo et al. 2009). This agreement suggests that the September to May precipitation anomalies can be used as a proxy of the soil moisture anomalies in the FLOR experiments for which the soil moisture outputs have not been saved (Fig. 9c).

To estimate the respective roles played by the anomalies of JJA precipitation (Figs. 7a–c) and of soil moisture at the beginning of the summer (Figs. 8 and

⁵ As we are focusing on the midtroposphere moisture budget (defined as the 700–300-hPa atmospheric layer) and not on the entire atmospheric moisture budget, it would be more appropriate to talk about the vertical moisture flux anomalies across the 700- and 300-hPa isosurfaces rather than about evaporation and precipitation.

⁶ The latter have been computed, as for the models, from monthly mean values of the horizontal wind and humidity fields.

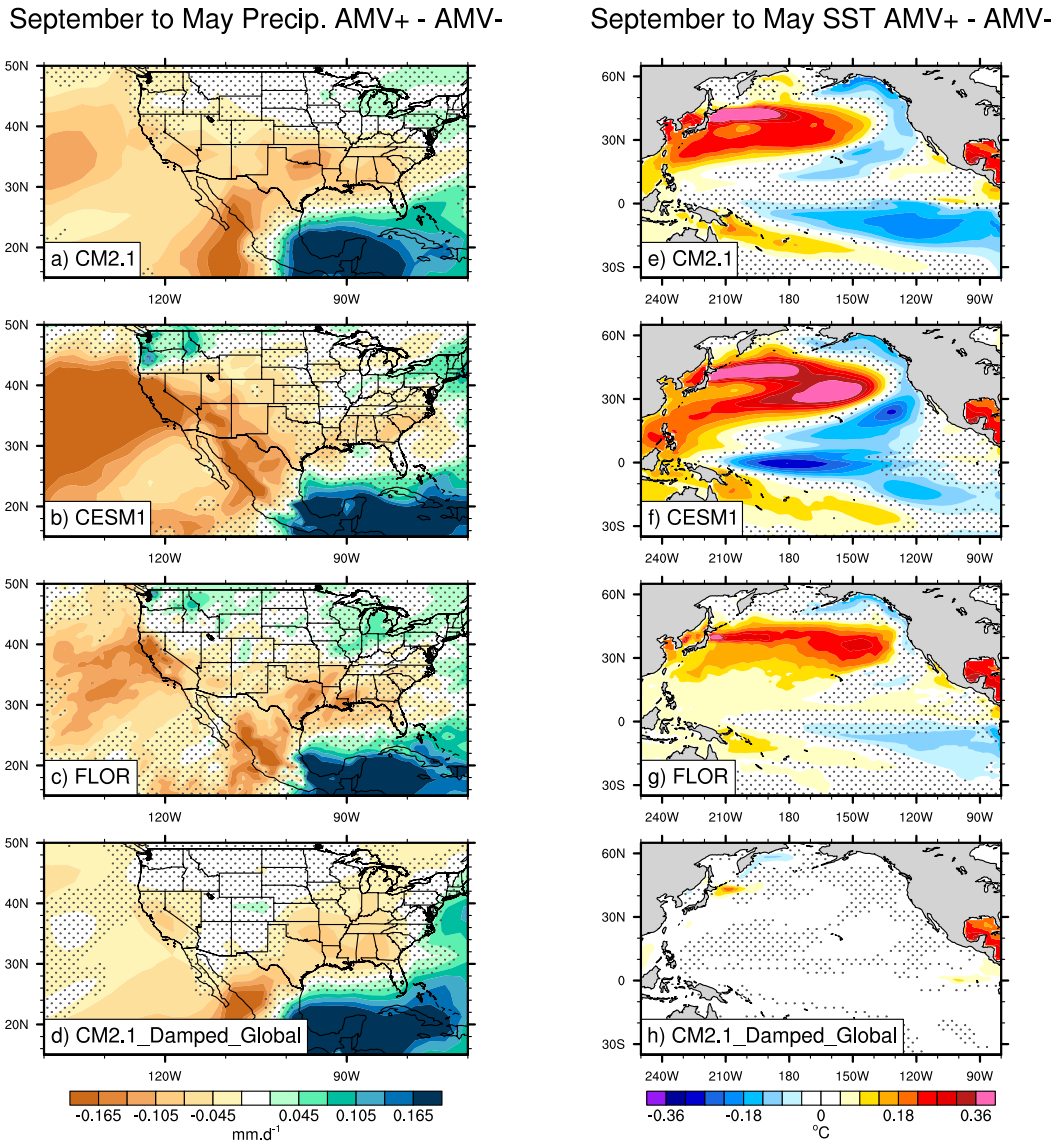


FIG. 9. Differences in 10-yr September–May average of (left) precipitation and (right) SST between AMV+ and AMV- experiments from (a),(e) CM2.1, (b),(f) CESM1, and (c),(g) FLOR. (d),(h) As in (a),(e), but for the CM2.1 Damped_Global_AMV experiments. Stippling indicates regions that are below the 95% confidence level of statistical significance according to a two-sided *t* test. Note that the effect of ocean–atmosphere coupling on the AMV impacts can be inferred by the differences between the first and the last row.

9a–c) on the anomalies of latent heat (Fig. 4) and on the number of heat wave days (Figs. 3b–d), we compute the uncentered⁷ pattern correlation between these maps (Table 1). We find that the pattern correlation between

the anomalies of May soil moisture and JJA latent heat are similar to the pattern correlation between JJA precipitation and JJA latent heat (multimodel mean correlation of -0.68 vs -0.69 , respectively). This suggests that the JJA precipitation and the May soil moisture anomalies play similar contribution in the JJA latent heat response to AMV. However, the correlation between the anomalies of the number of heat wave days and of May soil moisture is much stronger than that between the number of heat wave days and the JJA precipitation anomalies (multimodel mean

⁷ We use here the uncentered correlation to take into account the link between the variables coming both from the spatial mean shift and from the regional variations, in contrast to the centered correlation that only captures the links between the regional variations.

TABLE 1. Uncentered pattern correlation computed between, on one hand, an anomaly map of the latent heat and the number of heat wave days and, on the other hand, the JJA precipitation, the May soil moisture, the September–May precipitation, and the annual mean precipitation anomaly map for the region over which the number of heat wave days changes (20° – 45° N, 125° – 95° W). The values in the table are, from left to right, the correlation values from CM2.1, CESM1, and FLOR, and the intermodel correlation mean (in boldface; computed using Fisher transformation). The values in parentheses in the latent heat–May soil moisture box indicate the pattern correlation between the May soil moisture anomalies and the September–May precipitation anomalies, and the “x” indicates the absence of data from FLOR.

	JJA precipitation	May soil moisture	September–May precipitation	Annual precipitation
Latent heat	–0.58, –0.76, –0.72, –0.69	–0.61, –0.74, x, –0.68 (0.72, 0.79, x, 0.76)	–0.61, –0.73, –0.53, –0.64	–0.76, –0.83, –0.72, –0.78
Heat wave days	–0.43, –0.67, –0.59, –0.57	–0.74, –0.84, x, –0.80	–0.79, –0.81, –0.75, –0.78	–0.81, –0.88, –0.84, –0.85

correlation of -0.80 vs -0.57 , respectively). These results suggest that the mean soil moisture anomalies at the beginning of the summer are playing a dominant role in the modulation of heat waves. We interpret this role as a preconditioning to the development of hot episodes in response to the AMV forcing.

In summary, we show that the increased number of heat wave days in response to AMV+ in our simulations is linked both to JJA precipitation deficit and to drier than usual soil conditions at the beginning of the summer. This suggests that the precipitation response to AMV occurring all year long is key for understanding the modulation of the number of heat wave

days by AMV. Indeed, the high pattern correlation between the number of heat wave days and annual mean precipitation (multimodel mean correlation of -0.85) demonstrates a strong relationship between these two fields (cf. Figs. 10a–c and Table 1). In the present study, the link between JJA precipitation and heat wave anomalies is not corroborated from observational estimates (Fig. 7d). However, computing an annual mean precipitation composite of the AMV in observations, we find a precipitation decrease over Mexico and over the United States, suggesting that JJA LH anomalies have also played a role in the observed changes.

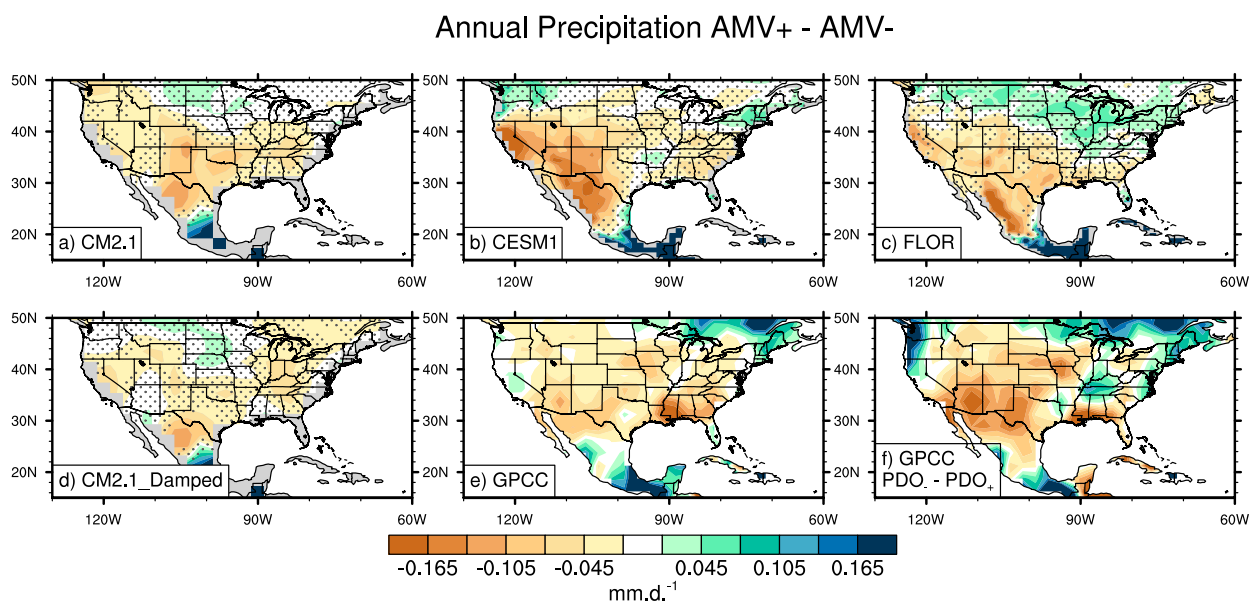


FIG. 10. Differences in 10-yr annual average precipitation between AMV+ and AMV– experiments from (a) CM2.1, (b) CESM1, and (c) FLOR. (d) As in (a), but for the CM2.1 Damped_Global_AMV experiments. (e) Observed precipitation composite difference between the positive and the negative years of the observed AMV index. (f) As in (e), but for a conditional composite taking into account both the observed AMV and PDO phases (see text for details). The observed precipitation data come from GPCC. Stippling in (a)–(d) indicates regions that are below the 95% confidence level of statistical significance according to a two-sided t test. The precipitation changes are shown for grid cells containing only surface area.

JJA Meridional humidity transport @925hPa AMV+ - AMV-

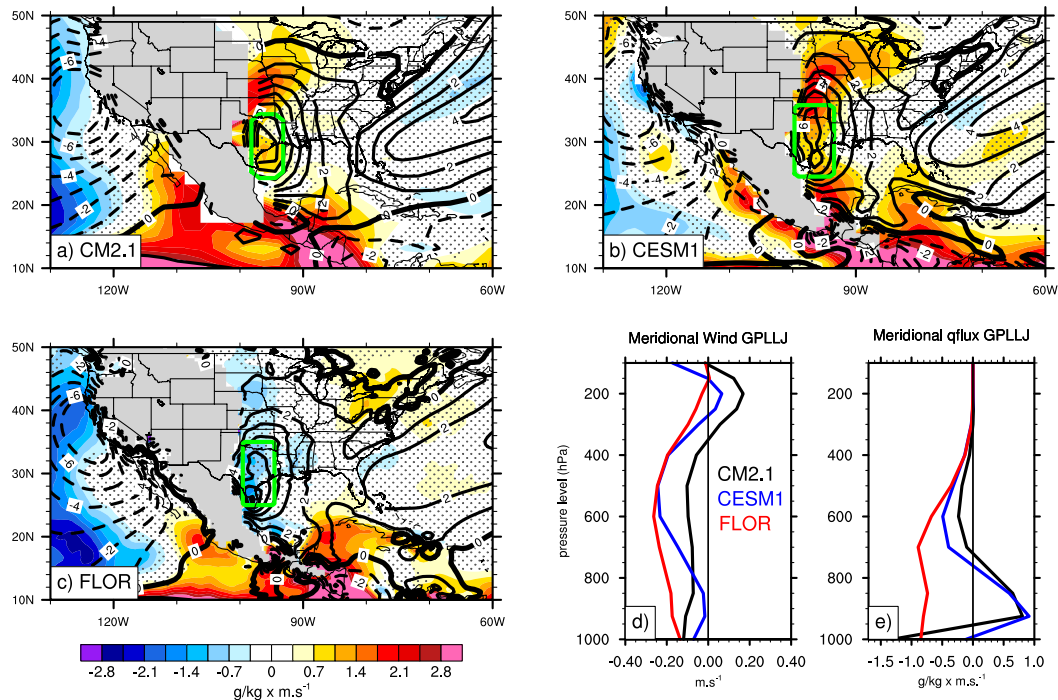


FIG. 11. JJA climatological meridional wind (contour interval of 1 m s^{-1} ; dashed contours indicate southward winds) and differences in 10-yr JJA average of meridional atmospheric humidity transport at 925 hPa (color shading) between AMV+ and AMV- experiments from (a) CM2.1, (b) CESM1, and (c) FLOR. Gray areas in (a)–(c) indicate regions where the isosurface at 925 hPa is not defined due to topography. Also shown are the atmospheric profile differences between the AMV+ and AMV- experiments of (d) meridional wind and (e) meridional humidity transport averaged over the Great Plains lower-level jet region indicated by the green contours in (a)–(c) for CM2.1 (black), CESM1 (blue), and FLOR (red). Stippling in (a)–(c) indicates regions that are below the 95% confidence level of statistical significance according to a two-sided t test.

c. Decreased downward longwave radiation

The LW_{dn} anomalies shown in Fig. 4 are consistent with the atmospheric humidity anomalies presented in Figs. 5a–c. As discussed in section 4a, the atmospheric drying over the western United States in response to AMV+ is partly explained by a divergence of humidity happening in the midtroposphere (Figs. 7e–g). Furthermore, looking at the lower troposphere, we find that humidity divergence is also happening off the California coasts (not shown), which could also explain part of the drying over the western United States. Over the eastern United States, the atmosphere tends to be wetter than usual, although discrepancies exist among the models on the magnitude of this wetting (Figs. 5a–c). In CM2.1 and CESM1, there is an increase of the meridional atmospheric moisture transport in the lower atmosphere over the Great Plains region, especially north of 30°N (Figs. 11a,b,e), whereas a decrease of this transport is simulated in FLOR (Figs. 11c,e). This difference in

moisture transport anomaly seems to explain the differences in the surface temperature, heat wave, and LW_{dn} responses, as well as in the atmospheric humidity anomalies over the central and eastern United States seen in Figs. 1b–d, 3b–d, 4, and 5a–c, respectively.

The difference in moisture transport response among the models may be due to differences in model mean states (cf. section 2b and Fig. S2). Indeed, FLOR has the weakest GPLLJ of the three CGCMs used in this study (cf. contours in Figs. 11a–c). The same atmospheric humidity anomaly over the Gulf of Mexico would then lead to a weaker anomaly of moisture transport by the mean flow in FLOR than in CM2.1 and CESM1. We note further that CESM1 is the CGCM simulating the most realistic GPLLJ mean state, whereas FLOR simulates a climatological GPLLJ maximum shifted to the south and it underestimates the northward extension of the jet. The mean bias of FLOR gives more credit to the moisture transport response to AMV simulated by CM2.1 and CESM1.

5. Discussion

a. The JJA precipitation anomalies

The JJA precipitation decrease over the central and western United States in response to AMV+ shown in Figs. 7a–c is consistent with the results of Sutton and Hodson (2007), Wang et al. (2008), and Kushnir et al. (2010), who estimated the climate impacts of a North Atlantic warming using atmosphere-only models forced by fixed SSTs. This suggests that using CGCM is not a prerequisite to represent these AMV impacts on summertime North America precipitation. Wang et al. (2008) and Feng et al. (2011) explain the precipitation deficit happening on the eastern flank of the Rocky Mountains by a decrease of the GPLLJ and of its associated moisture transport over the United States. We verify this mechanism in our experiments and find that the three models indeed simulate a decrease of the GPLLJ in response to AMV+ compared to AMV– conditions (Fig. 11d). However, we find that this effectively leads to a decrease of the northward moisture transport over the United States only in FLOR (Fig. 11e). In CM2.1 and CESM1, the moisture transport eventually strengthens due to an increase of the atmospheric moisture in response to the warm SST imposed over the North Atlantic.

Given that the three models show similar JJA precipitation anomalies over the United States, but disagree on the GPLLJ moisture transport response, we conclude that the changes in the GPLLJ moisture transport are not the main driver of the teleconnection between the AMV and U.S. precipitation in our simulations. We further conclude that these anomalies are mostly driven by the downward motion prevailing over northern Mexico and the southwestern United States (section 4a; Figs. 2e–g), and also potentially by evaporation–precipitation feedbacks north of 35°N (section 4b; Fig. S8). The primary role played by the increased downward motion on precipitation decrease over the United States in response to AMV+ has also been proposed by Sutton and Hodson (2007).

As stated in section 2f, a limitation of our analysis is that the atmospheric humidity transport and divergence have been computed from monthly wind and specific humidity outputs, which might lead to errors (e.g., Seager and Henderson 2013). A more detailed analysis would be needed to make stronger conclusions regarding the relationship between precipitation and atmospheric humidity divergence.

b. Role of the tropical Pacific adjustment to the AMV

The observed AMV composite of annual mean precipitation (Fig. 10e) shows some discrepancies with the simulated results (Figs. 10a–c). Both models and observations tend to show dry conditions over most of the

United States and northern Mexico associated with AMV+, but the maximum anomalies are localized over the southeastern United States in observations, whereas in our simulations the anomaly maxima are localized over the Sierra Madre Occidental (and California in CESM1). One possible explanation for the discrepancy between observation and modeled precipitation responses is that, in our simulations, the Pacific develops negative PDO-like SST anomalies during boreal winter in response to AMV warming [Figs. 9e–g; see also Ruprich-Robert et al. (2017) for detailed analysis of this teleconnection]. This Pacific response is likely modulating the direct AMV impacts on North American precipitation.

The relationship between AMV+ (AMV–) and a tropical Pacific cooling (warming) is not always verified in observations. Wu et al. (2011) and d'Orgeville and Peltier (2007) conclude from the historical records that the AMV leads the PDO by about a decade (with cold tropical Pacific anomalies following a warm AMV phase). Zhang et al. (2007) suggest that this time-lagged response comes from local air–sea interaction in the Pacific. Another explanation could be that internal Pacific variability may interfere with the Pacific response to the AMV forcing, making it difficult to isolate the AMV–Pacific relationship in observations. Indeed, the PDO appears to be not a single mode but rather the result of a combination of several physical processes (e.g., Newman et al. 2016), with the slowest components being possibly linked to AMV (cf. Fig. 7a in Newman et al. 2016). Following this perspective, one would need much longer observational records to robustly extract the AMV–Pacific and the AMV–North America teleconnections. Indeed, we stress here that the annual precipitation deficit shown in our experiments (Figs. 10a–c) is consistent with the results of Feng et al. (2011) based on paleodata, who estimated the anomalies of tree ring reconstructed Palmer drought severity index associated with the AMV (see Fig. 2b in Feng et al. 2011).

To determine whether the precipitation difference between the observed AMV composite and our simulations are coming from the Pacific SST response, we compute a conditional composite in observations. On one hand, we select years that fall both in the positive phase of the observed AMV and in the negative phase of the PDO (PDO–),⁸ and on the other hand we select years falling both in AMV– and PDO+ (Fig. 10f). The precipitation

⁸The PDO index is defined here from the 3-yr low-pass filtered principal component associated with the first EOF of the annual mean SST computed over the North Pacific sector (from 20° to 62°N) for the period 1901–2011. The 3-yr low-pass filter is used to minimize the impacts of interannual variability (such as ENSO) on the PDO composite.

anomalies of this conditional composite show stronger precipitation anomalies over North America than the nonconditional AMV composite (Fig. 10e), with maximum anomalies localized over northern Mexico and southwestern United States. These precipitation anomalies are more consistent with our simulations results (though still different), suggesting that the discrepancy between the observed and modeled precipitation response to AMV is partly coming from the Pacific response in our simulations.

The Damped_Global_AMV experiments performed with CM2.1 (cf. section 2c) also provide information on the role played by the SST response over the Pacific. In this experiment, the annual precipitation anomalies are reduced (Fig. 10d) compared to the CM2.1 AMV experiments (Fig. 10a) and show barely significant anomalies over the central United States. The anomalies in the number of heat wave days are also reduced in these experiments, in particular for the very extreme heat wave events (Fig. S11). These demonstrate that the adjustment of the Pacific Ocean plays a role in driving the impacts of the AMV over North America, in particular for the modulation of heat wave events. Most of the North American precipitation differences between the AMV and the Damped_Global_AMV experiments of CM2.1 occur from September to May, when the tropical Pacific cooling response to AMV is maximal (Fig. 9). This indicates that, in our simulations, 1) the non-summer precipitation anomalies over North America are partly driven by the Pacific response to the AMV forcing, 2) these precipitation anomalies lead to soil moisture anomalies, 3) the soil moisture anomalies are carried through to the summer, and 4) they act as a preconditioning for the development of heat waves.

6. Conclusions

Using three CGCMs (CM2.1, CESM1, and FLOR), we have investigated the North American climate response to the observed Atlantic multidecadal variability (AMV) during boreal summer. The large ensemble simulations performed in this study allows us to estimate the impacts of the AMV on the occurrence of weather extremes such as heat waves. For the three models, we find that an AMV warming leads on average to a precipitation deficit and a temperature warming over northern Mexico and the southwestern United States, as well as over the Great Plains in CM2.1 and CESM1. Furthermore, we find that the AMV modulates the number of heat wave days by about 30% over these regions. The mean temperature and precipitation impacts found in this study are in agreement with previous studies that used atmosphere-only models forced by Atlantic SST anomalies (Sutton and Hodson 2007; Wang

et al. 2008; Kushnir et al. 2010; Chylek et al. 2014), suggesting that these are robust impacts of the AMV. It also indicates that these AMV impacts are primarily driven by a direct atmospheric teleconnection between the North Atlantic and North America. However, we show evidence here that the ocean–atmosphere coupling, especially over the tropical Pacific, reinforces the North American summer climate response to AMV. In particular, using experiments inhibiting the Pacific SST response to AMV, we show that this coupling is needed to fully represent the modulation of heat waves by AMV.

We explore the physical mechanisms associated with the AMV teleconnections. As summarized in Fig. 12, we find that the impacts over northern Mexico and the southwestern United States are mostly driven by an increased atmospheric subsidence there, which is linked to a Matsuno–Gill-like response to the tropical Atlantic warming. This response leads to an atmospheric warming and to a horizontal atmospheric humidity divergence, which both drive a decrease of atmospheric relative humidity, cloud cover, and precipitation. This result is different from the studies of Wang et al. (2008) and Feng et al. (2011), who concluded that the decrease of the Great Plain low-level jet (GPLLJ) in response to AMV+ was responsible for the precipitation decrease over the United States. However, we find that the increased GPLLJ moisture transport in response to AMV+ in CM2.1 and CESM1 is responsible for the warming and the increased number of heat wave days over the Great Plains.

We find that the modulation by the AMV of the heat wave occurrence over northern Mexico and the southwestern United States is driven by three factors: an increase of solar irradiance in summer, a summer precipitation deficit, and a soil moisture deficit at the beginning of the summer. We speculate that the latter is acting as a preconditioning for the development of extreme temperatures during a heat wave event (e.g., Donat et al. 2016). The soil moisture anomalies are consistent with a precipitation deficit occurring from September to May over the region. We show that this precipitation deficit occurring outside the summer season is amplified by the Pacific Ocean adjustment to the AMV forcing, which leads to atmospheric changes and impacts northern America. These indirect AMV impacts highlight the desirability to use coupled models to fully capture the impacts of AMV on North America.

Given the potential predictability of the AMV, its teleconnections act as a source of predictability for the climate variations over land. Our results hence are encouraging for the prospect of getting skillful North American climate forecasts, and, in particular, for the prediction of the occurrence of heat waves at multiyear time scale. The three models used in this study have different land model,

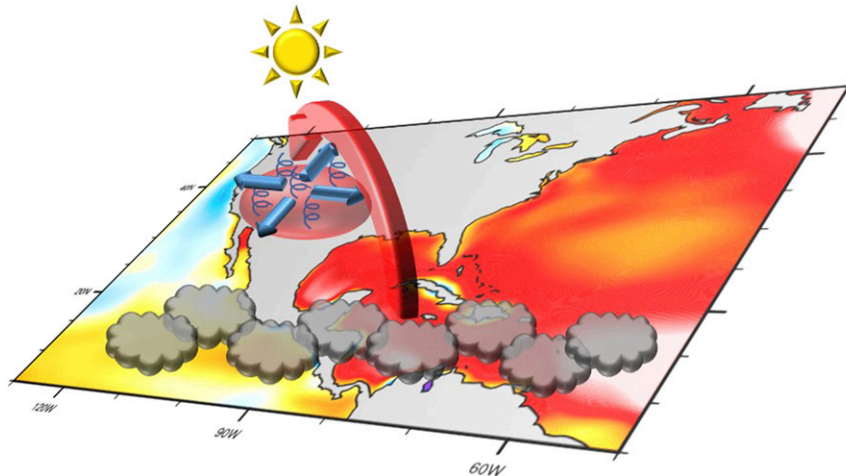


FIG. 12. Schematic of the mechanisms associated with the mean response of the summertime North American climate to a difference between the AMV+ and AMV− forcings. Positive North Atlantic SST anomalies (shading) increase deep atmospheric convection over the tropical Atlantic and eastern tropical Pacific (clouds), which drive an anomalous subsidence over the southwest of North America (curved red arrow). This subsidence leads to an anomalous midatmospheric mass and humidity divergence (blue arrows), and to less cloud cover and precipitation (sun). Altogether, the increase of solar radiation (through shortwave flux) and the lack of precipitation (through latent heat; blue streamers) lead to a warming of the surface and to an increase of the number of heat waves. Summertime latent heat anomalies are also coming from negative precipitation anomalies occurring all the year along—and integrated by the soil moisture—due to the La Niña-like response of the Pacific to the AMV forcing.

atmospheric physics, and atmospheric and land resolutions (from 200 to 50 km), but the overall results are very similar among the models. This consistency gives confidence about our results. However, the mean model biases in terms of soil moisture and surface air temperature, but also the representation of the land–atmosphere coupling and of the diurnal cycle precipitation, may interfere with the AMV impacts found in this study. Our conclusions therefore need to be corroborated with additional models. These could be done through component C of the Decadal Climate Prediction Project of the next phase of the Climate Model Intercomparison Project (Boer et al. 2016), which will include coordinated experiments similar to those discussed in the present study.

Acknowledgments. We thank Mingfang Ting for providing the AMV index used in this study; Sergey Malyshev, Salvatore Pascale, and Honghai Zhang for comments on an earlier version of the manuscript; and three anonymous reviewers who contributed to improve the quality of the manuscript through their constructive and helpful comments. The analysis and plots of this paper were performed with the NCAR Command Language (version 6.2.0, 2014), Boulder, Colorado (UCAR/NCAR/CISL/VETS, <http://dx.doi.org/10.5065/D6WD3XH5>). NCAR is sponsored by the National Science Foundation (NSF). The CESM is supported by

the NSF and the U.S. Department of Energy. This work is supported by the NSF under the Collaborative Research EaSM2 Grant OCE-1243015 to NCAR and by the NOAA Climate Program Office under the Climate Variability and Predictability Program Grant NA13OAR4310138 to NCAR and GFDL.

REFERENCES

- Alexander, L., 2011: Climate science: Extreme heat rooted in dry soils. *Nat. Geosci.*, **4**, 12–13, <https://doi.org/10.1038/ngeo1045>.
- Allan, R., and T. Ansell, 2006: A new globally complete monthly historical gridded mean sea level pressure dataset (HadSLP2): 1850–2004. *J. Climate*, **19**, 5816–5842, <https://doi.org/10.1175/JCLI3937.1>.
- Berg, A., B. R. Lintner, K. L. Findell, S. Malyshev, P. C. Loikith, and P. Gentine, 2014: Impact of soil moisture–atmosphere interactions on surface temperature distribution. *J. Climate*, **27**, 7976–7993, <https://doi.org/10.1175/JCLI-D-13-00591.1>.
- Boer, G. J., and Coauthors, 2016: The Decadal Climate Prediction Project (DCPP) contribution to CMIP6. *Geosci. Model Dev.*, **9**, 3751–3777, <https://doi.org/10.5194/gmd-9-3751-2016>.
- Changnon, S. A., K. E. Kunkel, and B. C. Reinke, 1996: Impacts and responses to the 1995 heat wave: A call to action. *Bull. Amer. Meteor. Soc.*, **77**, 1497–1506, [https://doi.org/10.1175/1520-0477\(1996\)077<1497:1ARTTH>2.0.CO;2](https://doi.org/10.1175/1520-0477(1996)077<1497:1ARTTH>2.0.CO;2).
- Chylek, P., M. K. Dubey, G. Lesins, J. Li, and N. Hengartner, 2014: Imprint of the Atlantic multi-decadal oscillation and Pacific decadal oscillation on southwestern US climate: Past, present, and future. *Climate Dyn.*, **43**, 119–129, <https://doi.org/10.1007/s00382-013-1933-3>.

- Ciais, P., and Coauthors, 2005: Europe-wide reduction in primary productivity caused by the heat and drought in 2003. *Nature*, **437**, 529–533, <https://doi.org/10.1038/nature03972>.
- Compo, G. P., and Coauthors, 2011: The Twentieth Century Reanalysis Project. *Quart. J. Roy. Meteor. Soc.*, **137**, 1–28, <https://doi.org/10.1002/qj.776>.
- Delworth, T. L., and Coauthors, 2006: GFDL's CM2 global coupled climate models. Part I: Formulation and simulation characteristics. *J. Climate*, **19**, 643–674, <https://doi.org/10.1175/JCLI3629.1>.
- Diffenbaugh, N. S., J. S. Pal, R. J. Trapp, and F. Giorgi, 2005: Fine-scale processes regulate the response of extreme events to global climate change. *Proc. Natl. Acad. Sci. USA*, **102**, 15 774–15 778, <https://doi.org/10.1073/pnas.0506042102>.
- Dole, R., and Coauthors, 2011: Was there a basis for anticipating the 2010 Russian heat wave? *Geophys. Res. Lett.*, **38**, L06702, <https://doi.org/10.1029/2010GL046582>.
- Donat, M. G., A. D. King, J. T. Overpeck, L. V. Alexander, I. Durre, and D. J. Karoly, 2016: Extraordinary heat during the 1930s US Dust Bowl and associated large-scale conditions. *Climate Dyn.*, **46**, 413–426, <https://doi.org/10.1007/s00382-015-2590-5>.
- Dong, B. W., R. T. Sutton, and A. A. Scaife, 2006: Multidecadal modulation of El Niño–Southern Oscillation (ENSO) variance by Atlantic Ocean sea surface temperatures. *Geophys. Res. Lett.*, **33**, L08705, <https://doi.org/10.1029/2006GL025766>.
- d'Orgeville, M., and W. R. Peltier, 2007: On the Pacific decadal oscillation and the Atlantic multidecadal oscillation: Might they be related? *Geophys. Res. Lett.*, **34**, L23705, <https://doi.org/10.1029/2007GL031584>.
- Douville, H., J. Colin, E. Krug, J. Cattiaux, and S. Thao, 2016: Midlatitude daily summer temperatures reshaped by soil moisture under climate change. *Geophys. Res. Lett.*, **43**, 812–818, <https://doi.org/10.1002/2015GL066222>.
- Easterling, D. R., J. L. Evans, P. Ya. Groisman, T. R. Karl, K. E. Kunkel, and P. Ambenje, 2000: Observed variability and trends in extreme climate events: A brief review. *Bull. Amer. Meteor. Soc.*, **81**, 417–425, [https://doi.org/10.1175/1520-0477\(2000\)081<0417:OVATIE>2.3.CO;2](https://doi.org/10.1175/1520-0477(2000)081<0417:OVATIE>2.3.CO;2).
- Enfield, D. B., A. M. Mestas-Núñez, and P. J. Trimble, 2001: The Atlantic multidecadal oscillation and its relation to rainfall and river flows in the continental U.S. *Geophys. Res. Lett.*, **28**, 2077–2080, <https://doi.org/10.1029/2000GL012745>.
- Feng, S., Q. Hu, and R. J. Oglesby, 2011: Influence of Atlantic sea surface temperatures on persistent drought in North America. *Climate Dyn.*, **37**, 569–586, <https://doi.org/10.1007/s00382-010-0835-x>.
- Fischer, E. M., S. I. Seneviratne, P. L. Vidale, D. Lüthi, and C. Schär, 2007: Soil moisture–atmosphere interactions during the 2003 European summer heat wave. *J. Climate*, **20**, 5081–5099, <https://doi.org/10.1175/JCLI4288.1>.
- Gill, A. E., 1980: Some simple solutions for heat-induced tropical circulation. *Quart. J. Roy. Meteor. Soc.*, **106**, 447–462, <https://doi.org/10.1002/qj.49710644905>.
- Hansen, J., M. Sato, and R. Ruedy, 2012: Perception of climate change. *Proc. Natl. Acad. Sci. USA*, **109**, E2415–E2423, <https://doi.org/10.1073/pnas.1205276109>.
- Hayes, M., M. Svoboda, and D. A. Wilhite, 2000: Monitoring drought using the standardized precipitation index. *Drought: A Global Assessment*, Vol. I, D. A. Wilhite, Ed., Routledge, 168–180.
- Hodson, D. L. R., R. T. Sutton, C. Cassou, N. Keenlyside, Y. Okumura, and T. Zhou, 2010: Climate impacts of recent multidecadal changes in Atlantic Ocean sea surface temperature: A multimodel comparison. *Climate Dyn.*, **34**, 1041–1058, <https://doi.org/10.1007/s00382-009-0571-2>.
- Huang, J., and H. M. van den Dool, 1993: Monthly precipitation–temperature relations and temperature prediction over the United States. *J. Climate*, **6**, 1111–1132, [https://doi.org/10.1175/1520-0442\(1993\)006<1111:MPTRAT>2.0.CO;2](https://doi.org/10.1175/1520-0442(1993)006<1111:MPTRAT>2.0.CO;2).
- Jia, L., and Coauthors, 2016: The roles of radiative forcing, sea surface temperatures, and atmospheric and land initial conditions in U.S. summer warming episodes. *J. Climate*, **29**, 4121–4135, <https://doi.org/10.1175/JCLI-D-15-0471.1>.
- Kam, J., J. Sheffield, and E. F. Wood, 2014: Changes in drought risk over the contiguous United States (1901–2012): The influence of the Pacific and Atlantic Oceans. *Geophys. Res. Lett.*, **41**, 5897–5903, <https://doi.org/10.1002/2014GL060973>.
- Kay, J. E., and Coauthors, 2015: The Community Earth System Model (CESM) Large Ensemble Project: A community resource for studying climate change in the presence of internal climate variability. *Bull. Amer. Meteor. Soc.*, **96**, 1333–1349, <https://doi.org/10.1175/BAMS-D-13-00255.1>.
- Knight, J. R., R. J. Allan, C. K. Folland, M. Vellinga, and M. E. Mann, 2005: A signature of persistent natural thermohaline circulation cycles in observed climate. *Geophys. Res. Lett.*, **32**, L20708, <https://doi.org/10.1029/2005GL024233>.
- Koster, R. D., and Coauthors, 2004: Regions of strong coupling between soil moisture and precipitation. *Science*, **305**, 1138–1140, <https://doi.org/10.1126/science.1100217>.
- Kucharski, F., I. S. Kang, R. Farneti, and L. Feudale, 2011: Tropical Pacific response to 20th century Atlantic warming. *Geophys. Res. Lett.*, **38**, L03702, <https://doi.org/10.1029/2010GL046248>.
- Kunkel, K. E., R. A. Pielke, and S. A. Changnon, 1999: Temporal fluctuations in weather and climate extremes that cause economic and human health impacts: A review. *Bull. Amer. Meteor. Soc.*, **80**, 1077–1098, [https://doi.org/10.1175/1520-0477\(1999\)080<1077:TFIWAC>2.0.CO;2](https://doi.org/10.1175/1520-0477(1999)080<1077:TFIWAC>2.0.CO;2).
- Kushnir, Y., R. Seager, M. Ting, N. Naik, and J. Nakamura, 2010: Mechanisms of tropical Atlantic SST influence on North American precipitation variability. *J. Climate*, **23**, 5610–5628, <https://doi.org/10.1175/2010JCLI3172.1>.
- Lau, N.-C., and M. J. Nath, 2012: A model study of heat waves over North America: Meteorological aspects and projections for the twenty-first century. *J. Climate*, **25**, 4761–4784, <https://doi.org/10.1175/JCLI-D-11-00575.1>.
- Li, X., S.-P. Xie, S. T. Gille, and C. Yoo, 2015: Atlantic-induced pan-tropical climate change over the past three decades. *Nat. Climate Change*, **6**, 275–279, <https://doi.org/10.1038/nclimate2840>.
- Matsuno, T., 1966: Quasi-geostrophic motions in the equatorial area. *J. Meteor. Soc. Japan*, **44**, 25–43, https://doi.org/10.2151/jmsj1965.44.1_25.
- Mazdiyasi, O., and A. AghaKouchak, 2015: Substantial increase in concurrent droughts and heatwaves in the United States. *Proc. Natl. Acad. Sci. USA*, **112**, 11 484–11 489, <https://doi.org/10.1073/pnas.1422945112>.
- McCabe, G. J., M. A. Palecki, and J. L. Betancourt, 2004: Pacific and Atlantic Ocean influences on multidecadal drought frequency in the United States. *Proc. Natl. Acad. Sci. USA*, **101**, 4136–4141, <https://doi.org/10.1073/pnas.0306738101>.
- McGregor, S., A. Timmermann, M. F. Stuecker, M. H. England, M. Merrifield, F.-F. Jin, and Y. Chikamoto, 2014: Recent Walker circulation strengthening and Pacific cooling amplified by Atlantic warming. *Nat. Climate Change*, **4**, 888–892, <https://doi.org/10.1038/nclimate2330>.
- Meehl, G. A., and C. Tebaldi, 2004: More intense, more frequent, and longer lasting heat waves in the 21st century. *Science*, **305**, 994–997, <https://doi.org/10.1126/science.1098704>.

- Mo, K. C., and R. W. Higgins, 1998: Tropical convection and precipitation regimes in the western United States. *J. Climate*, **11**, 2404–2423, [https://doi.org/10.1175/1520-0442\(1998\)011<2404:TCAPRI>2.0.CO;2](https://doi.org/10.1175/1520-0442(1998)011<2404:TCAPRI>2.0.CO;2).
- , and J. E. Schemm, 2008: Droughts and persistent wet spells over the United States and Mexico. *J. Climate*, **21**, 980–994, <https://doi.org/10.1175/2007JCLI1616.1>.
- , —, and S.-H. Yoo, 2009: Influence of ENSO and the Atlantic multidecadal oscillation on drought over the United States. *J. Climate*, **22**, 5962–5982, <https://doi.org/10.1175/2009JCLI2966.1>.
- Morice, C. P., J. J. Kennedy, N. A. Rayner, and P. D. Jones, 2012: Quantifying uncertainties in global and regional temperature change using an ensemble of observational estimates: The HadCRUT4 data set. *J. Geophys. Res.*, **117**, D08101, <https://doi.org/10.1029/2011JD017187>.
- Newman, M., and Coauthors, 2016: The Pacific decadal oscillation, revisited. *J. Climate*, **29**, 4399–4427, <https://doi.org/10.1175/JCLI-D-15-0508.1>.
- Pascale, S., S. Bordoni, S. B. Kapnick, G. A. Vecchi, L. Jia, T. L. Delworth, S. Underwood, and W. Anderson, 2016: The impact of horizontal resolution on North American monsoon Gulf of California moisture surges in a suite of coupled global climate models. *J. Climate*, **29**, 7911–7936, <https://doi.org/10.1175/JCLI-D-16-0199.1>.
- Robine, J.-M., S. L. K. Cheung, S. Le Roy, H. Van Oyen, C. Griffiths, J.-P. Michel, and F. R. Herrmann, 2008: Death toll exceeded 70,000 in Europe during the summer of 2003. *C. R. Biol.*, **331**, 171–178, <https://doi.org/10.1016/j.crv.2007.12.001>.
- Rohde, R., and Coauthors, 2013: A new estimate of the average Earth surface land temperature spanning 1753 to 2011. *Geoinf. Geostat. Overview*, **1**, <https://doi.org/10.4172/2327-4581.1000101>.
- Ross, T., and N. Lott, 2003: A climatology of 1980–2003 extreme weather and climate events. NCEP Tech. Rep. 2003-01, 14 pp., <https://www.ncdc.noaa.gov/billions/docs/lott-and-ross-2003.pdf>.
- Ruprich-Robert, Y., R. Msadek, F. Castruccio, S. Yeager, T. Delworth, and G. Danabasoglu, 2017: Assessing the climate impacts of the observed Atlantic multidecadal variability using the GFDL CM2.1 and NCAR CESM1 global coupled models. *J. Climate*, **30**, 2785–2810, <https://doi.org/10.1175/JCLI-D-16-0127.1>.
- Schlesinger, M. E., and N. Ramankutty, 1994: An oscillation in the global climate system of period 65–70 years. *Nature*, **367**, 723–726, <https://doi.org/10.1038/367723a0>.
- Schneider, U., A. Becker, P. Finger, A. Meyer-Christoffer, B. Rudolf, and M. Ziese, 2015: GPCC full data reanalysis version 6.0 at 2.5°: Monthly land-surface precipitation from rain-gauges built on GTS-based and historic data. Global Precipitation Climatology Centre, https://doi.org/10.5676/DWD_GPCC/FD_M_V7_250.
- Schubert, S. D., M. J. Suarez, P. J. Pegion, R. D. Koster, and J. T. Bacmeister, 2004: On the cause of the 1930s Dust Bowl. *Science*, **303**, 1855–1859, <https://doi.org/10.1126/science.1095048>.
- , and Coauthors, 2009: A U.S. CLIVAR project to assess and compare the responses of global climate models to drought-related SST forcing patterns: Overview and results. *J. Climate*, **22**, 5251–5272, <https://doi.org/10.1175/2009JCLI3060.1>.
- , H. Wang, and M. Suarez, 2011: Warm season subseasonal variability and climate extremes in the Northern Hemisphere: The role of stationary Rossby waves. *J. Climate*, **24**, 4773–4792, <https://doi.org/10.1175/JCLI-D-10-05035.1>.
- , and Coauthors, 2016: Global meteorological drought: A synthesis of current understanding with a focus on SST drivers of precipitation deficits. *J. Climate*, **29**, 3989–4019, <https://doi.org/10.1175/JCLI-D-15-0452.1>.
- Seager, R., and N. Henderson, 2013: Diagnostic computation of moisture budgets in the ERA-interim reanalysis with reference to analysis of CMIP-archived atmospheric model data. *J. Climate*, **26**, 7876–7901, <https://doi.org/10.1175/JCLI-D-13-00018.1>.
- , and M. Ting, 2017: Decadal drought variability over North America: Mechanisms and predictability. *Curr. Climate Change Rep.*, **3**, 141–149, <https://doi.org/10.1007/S40641-017-0062-1>.
- , N. Harnik, W. A. Robinson, Y. Kushnir, M. Ting, H.-P. Huang, and J. Velez, 2005a: Mechanisms of ENSO-forcing of hemispherically symmetric precipitation variability. *Quart. J. Roy. Meteor. Soc.*, **131**, 1501–1527, <https://doi.org/10.1256/qj.04.96>.
- , Y. Kushnir, C. Herweijer, N. Naik, and J. Velez, 2005b: Modeling of tropical forcing of persistent droughts and pluvials over western North America: 1856–2000. *J. Climate*, **18**, 4065–4088, <https://doi.org/10.1175/JCLI3522.1>.
- Smith, T. M., R. W. Reynolds, T. C. Peterson, and J. Lawrimore, 2008: Improvements to NOAA’s historical merged land–ocean surface temperature analysis (1880–2006). *J. Climate*, **21**, 2283–2296, <https://doi.org/10.1175/2007JCLI2100.1>.
- Sutton, R. T., and D. L. R. Hodson, 2005: North Atlantic forcing of North American and European summer climate. *Science*, **309**, 115–118, <https://doi.org/10.1126/science.1109496>.
- , and —, 2007: Climate response to basin-scale warming and cooling of the North Atlantic Ocean. *J. Climate*, **20**, 891–907, <https://doi.org/10.1175/JCLI4038.1>.
- Ting, M., Y. Kushnir, R. Seager, and C. Li, 2009: Forced and internal twentieth-century SST trends in the North Atlantic. *J. Climate*, **22**, 1469–1481, <https://doi.org/10.1175/2008JCLI2561.1>.
- , —, and C. Li, 2014: North Atlantic multidecadal SST oscillation: External forcing versus internal variability. *J. Mar. Syst.*, **133**, 27–38, <https://doi.org/10.1016/j.jmarsys.2013.07.006>.
- Trenberth, K. E., and G. W. Branstator, 1992: Issues in establishing causes of the 1988 drought over North America. *J. Climate*, **5**, 159–172, [https://doi.org/10.1175/1520-0442\(1992\)005<0159:IIECOT>2.0.CO;2](https://doi.org/10.1175/1520-0442(1992)005<0159:IIECOT>2.0.CO;2).
- , and C. J. Guillemot, 1996: Physical processes involved in the 1988 drought and 1993 floods in North America. *J. Climate*, **9**, 1288–1298, [https://doi.org/10.1175/1520-0442\(1996\)009<1288:PIIITD>2.0.CO;2](https://doi.org/10.1175/1520-0442(1996)009<1288:PIIITD>2.0.CO;2).
- , and D. J. Shea, 2005: Relationships between precipitation and surface temperature. *Geophys. Res. Lett.*, **32**, L14703, <https://doi.org/10.1029/2005GL022760>.
- Vecchi, G. A., and Coauthors, 2014: On the seasonal forecasting of regional tropical cyclone activity. *J. Climate*, **27**, 7994–8016, <https://doi.org/10.1175/JCLI-D-14-00158.1>.
- Wang, C., S.-K. Lee, and D. B. Enfield, 2008: Climate response to anomalously large and small Atlantic warm pools during the summer. *J. Climate*, **21**, 2437–2450, <https://doi.org/10.1175/2007JCLI2029.1>.
- Wittenberg, A. T., A. Rosati, N. C. Lau, and J. J. Ploshay, 2006: GFDL’s CM2 global coupled climate models. Part III: Tropical Pacific climate and ENSO. *J. Climate*, **19**, 698–722, <https://doi.org/10.1175/JCLI3631.1>.
- Wu, S., Z. Liu, R. Zhang, and T. L. Delworth, 2011: On the observed relationship between the Pacific decadal oscillation and the Atlantic multi-decadal oscillation. *J. Oceanogr.*, **67**, 27–35, <https://doi.org/10.1007/s10872-011-0003-x>.
- Zhang, R., T. L. Delworth, and I. M. Held, 2007: Can the Atlantic Ocean drive the observed multidecadal variability in Northern Hemisphere mean temperature? *Geophys. Res. Lett.*, **34**, L02709, <https://doi.org/10.1029/2006GL028683>.